JAMES | Journal of Advances in Modeling Earth Systems

RESEARCH ARTICLE
10.1029/2023MS003807

A New Eulerian Iceberg Module for Climate Studies

Olga Erokhina[1,2] and **Uwe Mikolajewicz**[1]

[1]Max Planck Institute for Meteorology, Hamburg, Germany, [2]Now at Astronomisches Rechen-Institut, Center for Astronomy of Heidelberg University, Heidelberg, Germany

Key Points:

- A new Eulerian iceberg module for climate studies is introduced
- The Eulerian approach simplifies the incorporation of icebergs into standard ocean general circulation models
- Experiments with a comprehensive climate model demonstrate that iceberg discharge has different impact on Atlantic meridional overturning circulation compared to freshwater

Correspondence to:
O. Erokhina,
olga.erokhina@uni-heidelberg.de

Citation:
Erokhina, O., & Mikolajewicz, U. (2024). A new Eulerian iceberg module for climate studies. *Journal of Advances in Modeling Earth Systems*, *16*, e2023MS003807. https://doi.org/10.1029/2023MS003807

Received 10 MAY 2023
Accepted 13 FEB 2024

Abstract Icebergs modulate the effective location of freshwater input from ice sheets into the ocean and therefore play an important role for the climate, especially during times of increased ice discharge (e.g., Heinrich events). None of the models participating in the Paleo Modeling Intercomparison Project simulations of the Last Glacial Maximum or the last deglaciation included icebergs. Here, we present a newly developed dynamic/thermodynamic iceberg module that was specifically designed to be incorporated in climate models used for long-term climate simulations with interactive ice sheets. In contrast to the widely used Lagrangian iceberg models, it is formulated in an Eulerian framework. This simplifies coupling to ocean models and enhances computational efficiency for glacial climates. In a set of sensitivity experiments, where the module was implemented into an Earth System Model, we validate the model for present-day climate conditions and test its sensitivity to key parameters. Further, we investigate the effect of iceberg hosing on the Atlantic meridional overturning circulation (AMOC) as compared to traditional freshwater hosing. Varying the hosing rate slowly in time yields a good approximation of the hysteresis curve of the AMOC. We find that the sensitivity of the AMOC to iceberg hosing is stronger than to freshwater hosing in the same ocean point, but weaker as compared to a latitude belt forcing in the North Atlantic. This emphasizes the 2e necessity to include interactive icebergs in long-term coupled climate simulations to realistically represent melt patterns and the response of the AMOC to freshwater input from melting ice sheets.

Plain Language Summary Icebergs transport frozen water from calving ice sheets far away from the coasts and release meltwater along their path while slowly melting. The sensitivity of the Atlantic meridional overturning circulation depends on the location of the meltwater input. As the transport and melt of icebergs determine the location of meltwater input into the ocean, it is obvious that icebergs are an important component of the climate system. Unfortunately, they are not included in most climate models, partly as they are computational quite expensive. Existing iceberg modules can follow groups of icebergs, and may be prohibitively computationally expensive when applied on very long timescales. Here we introduce a different approach. We do not follow each group of icebergs but describe the iceberg distribution using equations for concentrations and different size classes. This formulation is adequate for climate purposes, and simplifies the incorporation into ocean models. The difference in the climate response to iceberg calving and the widely used freshwater hosing is relatively large. This emphasizes the importance of including interactive iceberg modules into climate models for a realistic simulation of ice discharge events.

1. Introduction

Past rapid climate changes associated with a significant cooling in the North Atlantic realm occurred predominantly in glacial climates but also during glacial-interglacial transitions. It is widely thought that variations of the Atlantic meridional overturning circulation (AMOC) play a key role for such cooling events (Andrews & Voelker, 2018; Broecker, 1990; Heinrich, 1988; Kuniyoshi et al., 2022; Malmierca-Vallet et al., 2022; Ziemen et al., 2019). Several of these events are associated with the deposition of layers of ice rafted debris (mineral grains nearly sand size which are transported by icebergs and released to the ocean when icebergs melt) in large parts of the North Atlantic, termed Heinrich events (HEs, Heinrich, 1988). These events are caused by the episodic discharge of huge amounts of icebergs (e.g., Heinrich, 1988; Ruddiman, 1977) from the glacial ice sheets, predominantly the Laurentide ice sheet, and their subsequent drift across the North Atlantic. The meltwater from the icebergs reduces surface salinity and reduces or suppresses the formation of deep water and weakens the AMOC and the North Atlantic heat transport, leading to a substantial cooling. For the understanding of the role of HEs on climate, melting icebergs become particularly important, as the sensitivity of the AMOC to freshwater input depends on the location of the input (Condron & Winsor, 2012; Love et al., 2021; Maier-Reimer

& Mikolajewicz, 1989; Schiller et al., 1997; Swingedouw et al., 2022). Releasing icebergs from an ice sheet has a different effect on climate than releasing liquid melt water at the same location. In the latter case, the ocean surface salinity is diluted immediately, whereas icebergs drift and slowly release the melt water to the ocean at locations different than the original release site.

Hence, it is necessary to include an interactive iceberg module for long-term climate simulations, like transient simulations of the last deglaciation or even complete glacial cycles, when an interactive ice sheet component is used. Kapsch et al. (2022) concluded that the treatment of the freshwater flux is one of the biggest uncertainly in deglacial simulations. However, none of the models used for the deglacial climate simulations of phase 4 of the Paleo Model Intercomparison Project (Ivanovic et al., 2016) used interactive icebergs (e.g., Snoll et al., 2023).

As most climate models do not include interactive iceberg components, the effect of massive iceberg discharge has often been studied in climate models prescribing freshwater input either as a point source or as a spatially extended forcing in the North Atlantic (e.g., latitude belt forcing), mimicking the spatial pattern of the melting icebergs in a highly simplified manner (e.g., Ganopolski & Rahmstorf, 2001; Gregory et al., 2003; Hu et al., 2023; L. Jackson & Wood, 2018; L. C. Jackson et al., 2023; Kageyama et al., 2013; Maier-Reimer & Mikolajewicz, 1989; Mikolajewicz & Maier-Reimer, 1994; Otto-Bliesner & Brady, 2010; Peltier et al., 2006; Rahmstorf, 1996; Roche et al., 2014; Schiller et al., 1997; R. S. Smith & Gregory, 2009; Stouffer et al., 2006; Ziemen et al., 2019). To include at least the latent heat contribution associated with iceberg melt, calved icebergs were treated as an addition of sea-ice in simulations with a coupled atmosphere-ocean-ice sheet model focusing on HEs (Ziemen et al., 2014, 2019).

Within the PalMod project (www.palmod.de) we are working on the development of a coupled atmosphere-ocean-ice-solid earth model for the simulation of glacial cycles or significant fraction thereof. For this model system an iceberg component is obviously highly desirable. As our ocean model MPIOM does not contain an iceberg module, we decided to develop a new one particularly designed for the purpose of long-term climate simulations reaching from transient glacial climate simulations to simulations investigating the long-term effect of anthropogenic climate changes on the Antarctic ice sheet. The most important quantity of the iceberg module for this purpose is the addition of meltwater (and extraction of heat) from melting icebergs into the ocean. For the intended multi-millennial simulations low computational cost is also very important.

During the last decades several prognostic iceberg modules have been developed. They are formulated in a Lagrangian framework, tracking the evolution and decay of individual icebergs or group of icebergs. The very first modules considered either iceberg dynamics (e.g., Mountain, 1980; S. D. Smith, 1993) or thermodynamics (e.g., El-Tahan et al., 1987). The first iceberg module accounting for both thermodynamics and dynamics was developed by Bigg et al. (1997) and has been used as the basis for many iceberg modules that followed. A key application of iceberg modules has been in ship navigation, for which the correct prediction of iceberg trajectories is important to avoid hazards (e.g., Bigg & Wilton, 2014; Bigg et al., 1997, 2018; Keghouche et al., 2009; Mountain, 1980; S. D. Smith, 1993; Turnbull et al., 2015).

Other iceberg studies have investigated the spatial pattern of meltwater release from icebergs to estimate their effect on the ocean circulation (e.g., Bigg et al., 2011; Fendrock et al., 2022; Gladstone et al., 2001; Jongma et al., 2013; Levine & Bigg, 2008; Marson et al., 2021; Martin & Adcroft, 2010; Schloesser et al., 2019; Wiersma & Jongma, 2010). Applications for present-day and future studies have focused on the Antarctic and Greenland regions (e.g., Marson et al., 2021; Martin & Adcroft, 2010; Schloesser et al., 2019). Paleo studies examined the importance of icebergs in connection with HEs or the 8.2 ka event (Bigg et al., 2011; Fendrock et al., 2022; Jongma et al., 2013; Levine & Bigg, 2008; Wiersma & Jongma, 2010). Several studies also compared the response of the system forced by iceberg input with a system forced by freshwater injection (Bigg et al., 2011; Fendrock et al., 2022; Jongma et al., 2013; Levine & Bigg, 2008; Wiersma & Jongma, 2010). Of particular interest was also the sensitivity of the ocean response to different iceberg release sites (Bigg et al., 2011; Levine & Bigg, 2008). All these studies underline the importance of including interactive iceberg modules in climate models for the adequate simulation of the climate response to abrupt iceberg discharge events.

In the last decade there were a couple of approaches to implement icebergs in an Eulerian formulation as a part of the sea-ice model (Comeau, 2013; Vaňková & Holland, 2017). Comeau (2013) designed a dynamical-thermodynamic iceberg module as a part of CICE (Community Ice CodE) in both, a Lagrangian and an Eulerian framework. This allowed evaluating the module performance. In the Eulerian framework, icebergs are

distributed between size categories, can melt, and can interact with sea-ice, but there are no other interactive earth system components. The evaluation of the two approaches reveals that the distribution of the iceberg meltwater flux follows the paths of the simulated iceberg. A set of experiments indicated the necessity to use several different size categories. Vaňková and Holland (2017) designed and evaluated an ice melange (a mixture of icebergs and sea-ice) module that is mainly aiming at modeling icebergs in narrow fjords. Their ice melange was formulated in a semi-Lagrangian framework as part of the sea-ice model (implemented via rheology). By the time of their study their approach was computationally rather expensive.

The coupling of a Lagrangian iceberg module to an Eulerian ocean model, particularly in a massively parallel environment, requires the development of additional infrastructure for parallelization. Moreover, computational costs strongly depend on the number of icebergs being tracked in the module (Hunke & Comeau, 2011; Levine & Bigg, 2008). For multi-millennial model set-ups with fully interactive ice sheets, the number of potential iceberg source locations strongly increases during glacial climates, rendering the application of Lagrangian iceberg modules computationally expensive, as the computational costs in a Lagrangian iceberg model increases with the number of active icebergs. Approaches to track groups of Lagrangian icebergs are very efficient for situations with a low number of active source locations. If grouping is additionally used to reduce the number of source locations this reduces the accuracy. This is likely a major reason for the low number of studies in climate research that use interactive iceberg components. In this paper, we present another approach to iceberg modeling for climate purposes through the formulation of an iceberg module in an Eulerian framework as a part of ocean model. This approach requires the discretization of the iceberg distribution in size classes. The decay of icebergs is described as a transfer from one iceberg size class to the next smaller size class that differs from the approach of Comeau (2013) where the remaining iceberg mass is distributed across smaller size categories. However, the Eulerian framework overcomes previous shortcoming of the Lagrangian approach by being computationally cheap and independent of the number of modeled icebergs and input locations. Moreover, it allows for a rather straightforward integration of the iceberg module into the infrastructure of parallel ocean models. The new modeling framework focuses on effects of icebergs that are particularly relevant for the climate, such as the addition of mass (meltwater) and heat into the ocean during iceberg melt.

In Section 2 of this paper we introduce our new Eulerian iceberg module and its coupling into the Max Planck Institute for Meteorology Earth System Model (MPI-ESM). In Section 3 we validate the model results and run sensitivity experiments to different parameters newly introduced in our formulation of Eulerian iceberg module.

In Section 4 a set of highly idealized multi-millennial experiments with a climate model including our interactive iceberg module is described and analyzed. These runs show the differences between AMOC response to iceberg calving and freshwater hosing and demonstrate, why an interactive iceberg module is important for many experiments.

2. Model Description

In the following we describe the MPI-ESM system, used for this study. This is followed by a detailed description of our Eulerian iceberg module, including the descriptions of iceberg dynamics and thermodynamics as well as the coupling to the ocean model component of MPI-ESM. A list with the symbols used throughout the sections is given in Table 1.

2.1. Max Planck Institute Earth System Model

We use the MPI-ESM (Mauritsen et al., 2019) consisting of the atmospheric component ECHAM6 (Stevens et al., 2013), the land subcomponent JSBACH (Reick et al., 2013), and the ocean component MPIOM (Jungclaus et al., 2013). The atmosphere and the ocean are coupled via the Ocean Atmosphere Sea Ice Soil coupler OASIS3 (Valcke, 2013) with a coupling step of one day.

ECHAM6 is an atmospheric general circulation model on mixed finite-difference/spectral discretization. The spectral horizontal resolution in a coarse resolution set-up corresponds to the triangular truncation at wave number 31 (T31, approximately 3.75° × 3.75° resolution in grid point space). The vertical discretization is implemented on 31 hybrid σ-pressure layers (L31) (Stevens et al., 2013). The dynamical vegetation model JSBACH is a part of ECHAM6 and runs on the same grid (Reick et al., 2013; Schneck et al., 2013). The model is formulated using "plant functional types" where each grid cell is split into several "tiles" corresponding to

Table 1
List of Symbols and Parameters

Symbol	Description	Value	Units
A_{si}	Sea-ice concentration		m^{-2}
a	Wave amplitude		–
C	Iceberg concentration		m^{-2}
$c_{a,v}$	Vertical air drag coefficient	1.3	–
$c_{a,h}$	Horizontal air drag coefficient	0.0055	–
c_r	Wave radiation coefficient		–
$c_{si,v}$	Vertical sea-ice drag coefficient	0.9	–
$c_{w,v}$	Vertical water drag coefficient	0.9	–
$c_{w,h}$	Horizontal water drag coefficient	0.0012	–
$\vec{F}_a$	Air drag		kg m s^{-2}
$\vec{F}_{cor}$	Coriolis force		kg m s^{-2}
$\vec{F}_p$	Pressure gradient		kg m s^{-2}
$\vec{F}_r$	Wave radiation		kg m s^{-2}
$\vec{F}_{si}$	Sea-ice drag		kg m s^{-2}
$\vec{F}_w$	Water drag		kg m s^{-2}
$\vec{f}$	Coriolis parameter		s^{-1}
$\vec{g}$	Gravitational force	9.81	m s^{-2}
H	Iceberg height		m
$H_{\max}$	Maximal iceberg height		m
H_{si}	Sea-ice thickness		m
k	Ocean layer index		–
k_{bot}	Ocean layer index corresponding to the bottom of the iceberg		–
k_{sf}	Ocean layer index corresponding to the ocean surface		–
L	Iceberg length		m
L_c	Cutoff length		m
L_t	Upper limit of cutoff length		m
L_w	Wave length		m
M_{bas}	Basal melt		m s^{-1}
M_{bc}	Melting due to buoyant convection		m s^{-1}
M_{we}	Melting due to wave erosion		m s^{-1}
N	Total number of iceberg size classes in the module		–
n	Iceberg size class		–
Ω	Earth rate of rotation		s^{-1}
P	Measure of resistance of sea-ice		N m^{-2}
P^*	Sea-ice strength threshold value	20,000	N m^{-2}
ϕ	Latitude		rad
ρ_{ice}	Ice density	1,000	kg m^{-3}
ρ_{si}	Sea-ice density	910	kg m^{-3}
ρ_a	Air density	1.3	kg m^{-3}
ρ_w	Water density	1,025	kg m^{-3}
R	Iceberg melt rate		m^3 s^{-1}
s_{calv}	Ice sheet calving flux		m s^{-1}

Table 1
Continued

Symbol	Description	Value	Units
S_s	Sea state function		–
T_{freeze}	Ocean freezing temperature	−1.9	°C
T_{ib}	Iceberg temperature	−4.0	°C
T_{sf}	Ocean surface temperature		°C
T_w	Ocean temperature		°C
t	Time		s
V	Iceberg volume		m^3
$V_{\max}$	Volume of the biggest iceberg size class		m^3
$V_{\max\_observed}$	Volume of the biggest observed iceberg size class		m^3
V_{mim}	Volume of the smallest iceberg size class		m^3
$\vec{v}$	Iceberg velocity		m s^{-1}
$\vec{v}_a$	Air velocity		m s^{-1}
$\vec{v}_{dr}$	Iceberg drift velocity		m s^{-1}
$\vec{v}_{sf}$	Ocean surface velocity		m s^{-1}
$\vec{v}_{si}$	Sea-ice velocity		m s^{-1}
$\vec{v}_w$	Ocean velocity		m s^{-1}
W	Iceberg width		m
$W_{\min}$	Minimal iceberg width		m
ζ	Sea surface elevation		m

different dynamically changeable vegetation types. The water budget over land is closed by the river runoff module HD (Hagemann & Dümenil, 1997).

MPIOM is a primitive-equation ocean general circulation model on a z-coordinate system (Jungclaus et al., 2006, 2013; Marsland et al., 2003). The spatial discretization is implemented on a curvilinear Arakawa C-grid (Arakawa & Lamb, 1977). It has a free surface and includes a thermodynamic-dynamic sea-ice model with viscous-plastic rheology (Hibler, 1979).

To design and test the iceberg module, we use the stand-alone ocean model MPIOM at different resolutions. A set-up with horizontal resolution of 1.5° (GR15) is used for ocean-only simulations to test the iceberg component (see Section 3). The coarse resolution set-up (CR), which has a formal resolution of 3° (GR30), is applied for the coupled simulations in Section 4. For both configurations, the model grid poles are located in southeast Greenland and near the center of Antarctica. These locations were chosen in order to have relatively high resolution in areas where deep water formation typically occurs. In all set-ups, the ocean has 40 unevenly distributed vertical levels (L40) with 9 levels in the upper 100 m. Below this, the layer thickness increases with depth.

Sea surface temperature (SST), sea-ice thickness and concentrations, snow thickness, and ocean surface velocity are transferred from MPIOM to ECHAM6. Wind stress components over ocean and sea ice, liquid and solid freshwater fluxes, heat fluxes over the ocean and ice, heat flux residual, net short wave radiation and wind speed are transferred from ECHAM6 to MPIOM.

The MPI-ESM-CR model has been initialized with preindustrial restart files from a deglacial transient simulation introduced in Kapsch et al. (2022). The set-up was generated with an automated procedure based on the algorithms for ocean bathymetry generation by Meccia and Mikolajewicz (2018). The river direction file has been generated as described in Riddick et al. (2018).

2.2. The Eulerian Iceberg Module

In the Lagrangian approach (e.g., Bigg et al., 1997; Martin & Adcroft, 2010), individual groups of icebergs are considered and tracked with typical state variables such as iceberg dimension (length, width, and height), position

(latitude and longitude) and velocities. Whereas in the Lagrangian framework a continuous distribution of iceberg sizes is modeled, the size distribution in the Eulerian framework needs to be discretized. Instead of the properties of individual icebergs, iceberg concentrations for different size classes are main state vectors in the Eulerian approach. Changes in iceberg size result in a transition between iceberg size classes with matching changes in concentrations. Therefore, in the Eulerian approach, prognostic variables are iceberg concentration, as well as iceberg velocities for every iceberg size class on each grid box.

For simplicity, we use a 1D size class distribution with iceberg volume as the only variable. For each volume class, fixed values of length, width and height are defined. In principle, the module could easily be extended into a 2D (area and depth) or a 3D (length, width, and depth) iceberg size class distribution. However, the computational cost would increase substantially. As an additional simplification, the direct interaction between icebergs is neglected, which is also frequently assumed in Lagrangian iceberg modules (e.g., Martin & Adcroft, 2010).

In our Eulerian iceberg module, the iceberg distribution is described by concentrations $C(n)$ of N iceberg size classes ($n = 1; N$) with a known volume $V(n)$ at every ocean grid box over the entire ocean domain. The total number of icebergs is given by the area integral over the concentrations for all size classes. Icebergs move with velocities $\vec{v}(n)$. Changes in iceberg concentration $C(n)$ are due to the horizontal advection, the transfer of icebergs from one size class n to the adjacent classes ($n \pm 1$; the module's representation of iceberg melt and growth), as well as the generation of new icebergs due to the ice sheet calving $s_{calv}(n)$. For the calculation of iceberg velocities and melting the same set of parameterizations as in the Lagrangian formulation can be used. Beside the iceberg state, these parameterizations use the oceanic and the atmospheric state at every time step. Iceberg melt rate $R(n)$ is calculated after the calculation of iceberg velocities, as the melt rate depends on iceberg velocities. Melting is expressed by transferring a part of the bigger icebergs size class $C(n)$ to the next smaller iceberg size class $C(n-1)$. Only discharge from calving locations is allowed to increase the total number of icebergs and only melt in the smallest iceberg size class can result in a decrease in the total number of icebergs. Therefore, the evolution of iceberg concentration for every iceberg size class is:

$$\frac{\partial C(n)}{\partial t} + \nabla \cdot \left(\vec{v}(n) C(n) \right) = -\frac{C(n)R(n)}{V(n) - V(n-1)} + \frac{C(n+1)R(n+1)}{V(n+1) - V(n)} + \frac{s_{calv}(n)}{V(n)} \tag{1}$$

where n—is an iceberg size class ($n = 1; N$), N is the total number of iceberg size classes in the module, $C(n)$ is the iceberg concentration of size class n, $V(n)$ is the volume of an individual iceberg of size class n, $R(n)$ is the melt rate of an iceberg of size class n, $s_{calv}(n)$ is the ice sheet calving rate released to an iceberg size class n. In the following, the iceberg size class index n is omitted in the equations for simplicity.

Key components, which describe iceberg properties after the calving from the ice sheet, are based on studies by Bigg et al. (1997) and modifications by Martin and Adcroft (2010) and are discussed below.

2.2.1. Iceberg Dynamics

In this section, we describe the iceberg drift in details. The basic equation for iceberg drift was suggested by Bigg et al. (1997) and has been widely used in other studies (e.g., Gladstone et al., 2001; Jongma et al., 2013; Martin & Adcroft, 2010). Changes in the drift velocity $\vec{v}$ are driven by the wind, sea-ice drift, ocean currents, waves and the sea slope:

$$\rho_{ice} V \frac{\partial \vec{v}_{dr}}{\partial t} = \vec{F}_a + \vec{F}_w + \vec{F}_{si} + \vec{F}_r + \vec{F}_p + \vec{F}_{cor} \tag{2}$$

where ρ_{ice} is the density of ice, $\vec{F}_a$ is the air drag, $\vec{F}_w$ is the water drag, $\vec{F}_{si}$ is the sea-ice drag, $\vec{F}_r$ is the wave radiation force, $\vec{F}_p$ is the pressure gradient, and $\vec{F}_{cor}$ is the Coriolis force.

In our iceberg module we neglect the advection of momentum appearing as a separate term in the Eulerian formulation, which is justified due to coarse resolution, for which the effects of ocean/sea-ice velocity and the wind forcing are dominant

1. The first term of the force balance is air drag $\vec{F}_a$. The subaerial part of the iceberg (sail) is pushed by the wind. The drag is proportional to the square of the iceberg-air relative velocity as in Bigg et al. (1997) with the modification by Martin and Adcroft (2010):

$$\vec{F}_a = \rho_a(0.5\ c_{a,v}WH_s + c_{a,h}LW)\left|\vec{v}_a - \vec{v}\right|\left(\vec{v}_a - \vec{v}\right) \tag{3}$$

where ρ_a is the density of air, W and L are the iceberg width and length, H_s is the sail height, $c_{a,v}$ and $c_{a,h}$ are the vertical and horizontal air drag coefficients, respectively, and $\vec{v}_a$ is the air velocity.

2. The second term is the water drag $\vec{F}_w$. The submerged iceberg part (keel) is affected by ocean currents (Martin & Adcroft, 2010) and is calculated separately for each of the ocean model layers (S. D. Smith, 1993):

$$\begin{aligned}\vec{F}_w = \ & \rho_w \sum_{k=1}^{k_{bot}}(0.5\ c_{w,v}WH(k) + c_{w,h}LW)\left|\vec{v}_w(k) - \vec{v}\right|\left(\vec{v}_w(k) - \vec{v}\right) - \\ & -\rho_w 0.5\ c_{w,v}WH_{si}\left|\vec{v}_{sf} - \vec{v}\right|\left(\vec{v}_{sf} - \vec{v}\right)\end{aligned} \tag{4}$$

where ρ_w is the water density, k is the ocean layer index ($k = 1$; k_{bot}), k_{bot} is the ocean layer index corresponding to the bottom of the iceberg, W and L are the iceberg width and length, $H(k)$ is the height of the iceberg in the ocean layer k, H_{si} is the sea-ice thickness, $c_{w,v}$ and $c_{w,h}$ are the vertical and horizontal water drag coefficients, $\vec{v}_w$ is the ocean velocity of the ocean layer k ($k = k_{sf} = 1$ is the surface ocean velocity).

3. The third term is the sea-ice drag $\vec{F}_{si}$. The top of the submerged part of an iceberg can be pushed by sea-ice. The classical approach (Bigg et al., 1997) is modified to make it possible to account for the concentration of sea-ice:

$$\vec{F}_{si} = 0.5\ A_{si}\ \rho_{ice}c_{si,v}WH_{si}\left|\vec{v}_{si} - \vec{v}\right|\left(\vec{v}_{si} - \vec{v}\right) \tag{5}$$

where ρ_{si} is the sea-ice density, A_{si} is the sea-ice concentration, W is the iceberg width, H_{si} is the sea-ice thickness, $c_{si,v}$ is the vertical sea-ice drag coefficients, $\vec{v}_{si}$ is the sea-ice velocity.

4. The fourth term is the wave radiation force $\vec{F}_r$. Each iceberg is also affected by incident waves that push it in addition to the air drag force. We use here the parameterization given in Martin and Adcroft (2010):

$$\vec{F}_r = 0.5\ \rho_w c_r a\vec{g}\ \min(a, H_s)\ \frac{2LW}{L+W}\frac{\vec{v}_a}{\left|\vec{v}_a\right|} \tag{6}$$

where ρ_w is the water density, $\vec{g}$ is the Earth gravity, H_s is the sail height, W and L are the iceberg width and length, $\vec{v}_a$ is the air velocity, a is the wave amplitude $a = 0.010125\left|\vec{v}_a - \vec{v}\right|^2$ and the wave radiation coefficient

$$c_r = 0.06\ \min\left(\max\left[0, \frac{L - L_c}{L_f - L_c}\right], 1\right) \tag{7}$$

where the cutoff length is $L_c = 0.125L_w$ and the upper limit is $L_t = 0.25L_w$, with a wave length of $L_w = 0.32\left|\vec{v}_a - \vec{v}\right|^2$.

5. The fifth term is the pressure gradient $\vec{F}_p$. The pressure gradient is a basic force that has influences on any object in the water due to difference in the sea level height:

$$\vec{F}_p = -m\vec{g}\ \vec{\nabla}\zeta \tag{8}$$

where $\vec{g}$ is the Earth gravity, ζ is the sea surface elevation, m is the iceberg mass.

6. The sixth term is Coriolis force $\vec{F}_{cor}$. The Coriolis term describes the effect of rotation of the Earth:

$$\vec{F}_{cor} = -m\vec{f} \times \vec{v} \tag{9}$$

where f is the Coriolis parameter,

$$f = 2\ \Omega\ \sin(\phi) \tag{10}$$

and Ω is the Earth rate of rotation and ϕ is the latitude in radians, m is the iceberg mass.

The solution of Equation 2 is the drift velocity $\vec{v}_{dr}$. The final iceberg velocity $\vec{v}$ depends on the sea-ice concentration A_{si} and sea-ice characteristic in the grid cell (P is the measure of the resistance of sea-ice and P^* is the sea-ice strength threshold value (Hibler, 1979) derived from observations, Keghouche et al., 2009). If the sea-ice concentration A_{si} is ≤90%, the iceberg velocity is exactly the drift velocity in Equation 2. For higher sea-ice concentration and strength, the iceberg is blocked by sea-ice and moves with its velocity ($A_{si} \geq 90\%$ and $P \geq P^*$; Hunke & Comeau, 2011; Keghouche et al., 2009). In order to make the transition between the two regimes smoother we apply a linear combination dependent on sea-ice strength between calculated iceberg drift velocity and iceberg velocity equal to the sea-ice velocity when sea-ice concentration is high ($A_{si} \geq 90\%$):

$$\vec{v} = \begin{cases} \vec{v}_{dr} & \text{if } A_{si} \leq 90\% \\ \dfrac{P\ \vec{v}_{dr} + P^*\ \vec{v}_{si}}{P + P^*} & \text{if } A_{si} > 90\% \\ \vec{v}_{si} & \text{if } A_{si} > 90\% \text{ and } P \geq P^* \end{cases} \tag{11}$$

where P is derived from

$$P = P^* H_{si} \exp(-20\ (1 - A_{si})). \tag{12}$$

2.2.2. Iceberg Thermodynamics

The main effects responsible for iceberg melt are wave erosion, bottom melt, and buoyant convection. To model the thermodynamics of icebergs, we use a 1D size distribution that is based on iceberg volume. Each volume class, length, width, and height (or vertical extension) are set a priori. The melt rate, R, is given by

$$R = (-LWM_{bas} - H(L + W)\,(M_{we} + M_{bc})) \tag{13}$$

where L, W, and H are the length, the width and the height of an iceberg, M_{bas} is the basal melt, M_{we} and M_{bc} are melting due to the wave erosion and the buoyant convection of an iceberg, respectively. Other melting components, like melt due to solar radiation on the iceberg surface or air forced convection on iceberg sides, are not included as they have only a minor contribution to the total iceberg melt (Bigg et al., 1997; El-Tahan et al., 1987; Martin & Adcroft, 2010).

1. The first term of the mass balance is the wave erosion M_{we}. The melting due to surface wave erosion on the iceberg walls at water level is a function of sea state, sea-ice coverage and SST (Martin & Adcroft, 2010). Here we modify the parametrization used by Martin and Adcroft to directly include the ocean freezing temperature:

$$M_{we} = \frac{1}{12} S_s \left(1 + \cos\left(\pi A_{si}^3\right)\right)\left(T_{sf} - T_{freeze}\right) \tag{14}$$

where T_{sf} is the SST, T_{freeze} is the ocean freezing temperature (−1.9°C), A_{si} is the sea-ice concentration, S_s is the sea state function calculated in accordance with the Beaufort scale (Martin & Adcroft, 2010):

$$S_s = \frac{3}{2}\left|\vec{v}_a - \vec{v}_w(k_{sf})\right|^{0.5} + \frac{1}{10}\left|\vec{v}_a - \vec{v}_w(k_{sf})\right|\left|\vec{v}_a - \vec{v}_w(k_{sf})\right|\left|\vec{v}_a - \vec{v}_w(k_{sf})\right| \quad (15)$$

Here $\vec{v}_a$ and $\vec{v}_w$ are air and water velocities, respectively; k_{sf} is the index of the surface ocean layer (sf = 1). The wave erosion component also accounts for the calving of the overhanging slabs.

2. The second term is the basal melt M_{bas}. The basal melt is driven by the turbulent flow at the base of the iceberg and is a function of the velocity and temperature difference between the ocean and iceberg (Bigg et al., 1997):

$$M_{bas} = 0.58\left|\vec{v} - \vec{v}_w(k_{bot})\right|^{0.8}\frac{T_w(k_{bot}) - T_{ib}}{L^{0.2}} \quad (16)$$

where $\vec{v}_w$ is the water velocity, k_{bot} the ocean layer index corresponding to the iceberg bottom, T_w is the temperature of the corresponding ocean layer, T_{ib} is the iceberg temperature (−4.0°C), L is the iceberg length. The basal melt for the grounded iceberg is set to zero.

3. The third term is buoyant convection M_{bc}. The buoyant convection is the melt along the keel walls of the iceberg that is driven by the quadratic function of the temperature difference between the iceberg and the ocean (El-Tahan et al., 1987). The buoyant convection is calculated independently for every ocean layer:

$$M_{bc} = \sum_{k=1}^{k_{bot}}\left(7.62\times10^{-3}T_w(k) + 1.29\times10^{-3}T_w^2(k)\right)\frac{H(k)}{H_k} \quad (17)$$

Here T_w is the ocean temperature of the layer k, k is the ocean layers index ($k = 1; k_{bot}$), k_{bot} is the ocean layer index corresponding to the iceberg bottom, $H(k)$ the height of the iceberg in the ocean layer k, and H_k the iceberg keel height.

2.2.3. Iceberg Size Distribution

Whereas in Lagrangian modules only the size distribution of the iceberg input needs to be specified, and the simulated iceberg size distribution is a continuum, the Eulerian formulation requires a predefined discrete size distribution for the entire iceberg population. Therefore, in the Eulerian framework, the iceberg shape (length, width and height), is not a prognostic quantity (as e.g., in Martin & Adcroft, 2010) but needs to be discretized and thus specified a priori. Whereas in Lagrangian modules iceberg melt is described as a change in volume, the Eulerian formulation describes melt as transfer from one size class to the next smaller one.

For simplicity we chose a 1D distribution (only volume, the three spatial dimensions are prescribed for each size class). A 1D approach has also been used in some Lagrangian iceberg modules (e.g., El-Tahan et al., 1987; Kubat et al., 2007).

For the iceberg source from calving ice sheets the distribution given by Bigg et al. (1997) is widely used (hereafter referred to as BIGG input function). The BIGG input function is based on studies on the iceberg sizes distribution for present-day from observational data in the Northern Hemisphere (e.g., Dowdeswell & Forsberg, 1992; Weeks & Mellor, 1978). These studies showed that the distribution follows a log-normal function of length. In a Lagrangian module, Bigg et al. (1997) included 10 different iceberg size classes and excluded large icebergs (bigger than 1,000 m in length; Table 1 in Bigg et al., 1997). Typically this input size distribution is used for both hemispheres and different time periods (e.g., Levine & Bigg, 2008). We largely follow this approach.

The iceberg size distribution for the newly generated icebergs in an Eulerian approach follows the BIGG input function with a linear interpolation onto our size classes. Necessary input parameters required for the discretization are the total number of size classes N, and the volume of the biggest ($V_{\max}$) and the smallest ($V_{\min}$) icebergs, minimal iceberg width ($W_{\min}$), and maximal iceberg height ($H_{\max}$).

As we use a 1D size distribution, we have to specify a relation between width, length and height of the icebergs for each size class.

The iceberg length $L(n)$ is function of iceberg width $W(n)$ and is defined from a relation $L(n)$: $W(n)$ = 1.5:1, as in many Lagrangian iceberg modules (Bigg et al., 1997; Jongma et al., 2009; Rackow et al., 2017).

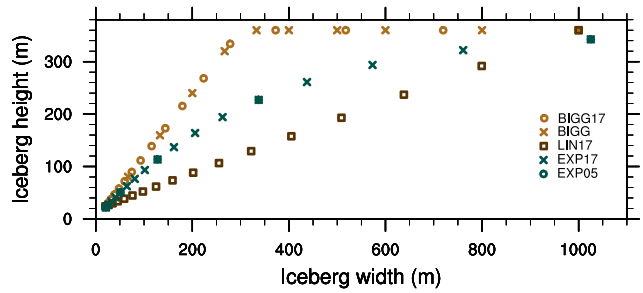

Figure 1. Iceberg height (m) versus iceberg width (m) with different parameterizations: brown circles display the BIGG input function (Bigg et al., 1997) with $N = 10$; brown crosses are a modified Bigg et al. parameterization with $N = 17$ (BIGG17); dark brown squares correspond to a linear parameterization with $N = 17$ (LIN17, Equation 22); green labels show the values for the exponential parameterization with crosses corresponding to EXP17 $N = 17$ and circles to EXP05 $N = 5$ (Equation 18). Values are calculated for $H_{\max} = 360$ m; $W_{\min} = 20$ m; and $V_{\min} = 14{,}400$ m^3.

Iceberg height $H(n)$ similar to iceberg length $L(n)$ is also a function of iceberg width $W(n)$. Here we assume an exponential dependence of iceberg height on its width (EXP):

$$H(n) = H_{\max}\left(1 - e^{-\frac{W(n)}{H_{\max}}}\right) \tag{18}$$

This parameterization was chosen from the following assumptions. The vertical distribution of the meltwater injection from an iceberg into the ocean has two peaks, one in the layer containing the bottom of the iceberg, the other in the surface layer. This is due to the fact that the dominant processes of melting are bottom melt and wave erosion (Bigg et al., 1997), correspondingly. In the BIGG input function, all input classes larger than 300 m in width have the same keel height (300 m). This would lead to an artificial strongly two-peaked vertical distribution of the meltwater flux. To reduce this problem we do not use the dimensions as in the BIGG input function but rather implement a fit to an exponential function, which yields a more smooth vertical distribution of the iceberg meltwater flux between the ocean surface and the bottom of the biggest icebergs size class (Figure 1). This plays potentially an important role for the ocean circulation changes caused by iceberg melt.

The volume of the biggest iceberg size class is specified to be the same as the volume of the biggest size class in the BIGG input function (Table 1 in Bigg et al., 1997 $V_{\max} = V_{\max\_observed}$).

To make it possible to account for small icebergs or "bergy bits," the volume of the smallest iceberg size class $V_{\min}$ is different from the volume of the smallest iceberg in the BIGG input function. It is specified as a function of the minimal iceberg width $W_{\min}$:

$$V_{\min} = 1.5 \times 1.2 \times W_{\min}^3 \tag{19}$$

where 1.5 corresponds to the ratio $L{:}W = 1.5$ and 1.2 follows from the ratio between height and width for small (up to 4) iceberg size classes in the BIGG input function (Bigg et al., 1997).

In our iceberg module, the ratio between the volumes of iceberg classes $V(n-1)$ and $V(n)$ is kept constant. Thus, specifying the smallest and the biggest iceberg size classes and the number of size classes N determines the volume of all other iceberg size classes (n is the iceberg size class, $n = 1; N$):

$$\frac{V(n)}{V(n-1)} = \left(\frac{V_{\max}}{V_{\min}}\right)^{\left(\frac{1}{n-1}\right)} \tag{20}$$

For the iceberg volume of each size class, the width, length and height are then calculated using the above-mentioned relations. In this study we use the following values: $V_{\min} = 14{,}400$ m^3, $V_{\max} = 5.4 \times 10^9$ m^3, $W_{\min} = 20$ m, $H_{\max} = 360$ m.

In addition to the exponential relation between iceberg width and height we have implemented in the model two other relation: a linear interpolation between the largest and smallest specified iceberg properties (LIN) and a linear interpolation between the properties of the neighboring size classes of the BIGG input function (BIGG). The effect on the spatial distribution of the simulated iceberg meltwater flux is discussed in Section 3.

2.2.4. Coupling to the Ocean Model

The coupling between the ocean model MPIOM and the Eulerian iceberg module is implemented by exchanging quantities for every time step. From the ocean model, the Eulerian iceberg module receives ocean potential temperature, salinity, velocity, sea-ice concentration, thickness and velocity, and sea surface elevation. From the atmosphere, the iceberg module receives wind speed and wind stresses, which are transferred via the OASIS3 coupler to MPIOM as part of the standard coupling. In our iceberg module, icebergs change only ocean water mass properties. The momentum transfer to ocean and sea ice through icebergs is neglected. Hunke and Comeau (2011) concluded from model simulations that this feedback effect is not relevant on climate-scale variables, so the feedback from icebergs on the ocean is restricted to the addition of mass (meltwater) and the extraction of heat. These feedbacks are implemented in 3D by injecting the meltwater into and extracting the heat required to melt iceberg from the respective ocean model layer. This has been implemented in a similar manner as in Wiersma and Jongma (2010), Jongma et al. (2013), Bügelmayer et al. (2015) and is more realistic than the coupling approaches that add iceberg fluxes only to the surface layer like for example, Jongma et al. (2009), Martin and Adcroft (2010), Marsh et al. (2015). There is no direct feedback from icebergs to the atmosphere.

The ocean model set-ups used here have a rather coarse resolution. Therefore, narrow fjords and their sill depths are not well represented. Releasing icebergs in these fjords (as it happens for some outlet glaciers), a grounding condition could lead to artificial accumulation of icebergs in the fjords due to the potentially too shallow representation of sills. This would affect the results obtained with this module. One way to avoid this problem would be to introduce icebergs only at the shelf edge and to transfer the iceberg sources further into the ocean. Another way could be to ensure that all fjords and channels have realistic sill depth. This could be done for a manually set up ocean model, but is practically not feasible for a transient deglacial simulation, where the ocean bathymetry and land-sea mask are generated automatically every 10 years (Meccia & Mikolajewicz, 2018), as planned in simulations with an interactive ice sheet component. Therefore we chose not to apply the classical grounding condition. However, at depths below the ocean bottom no transfer of heat or momentum is calculated. For high resolution set-ups, the problem does not occur, as the topography can adequately represent the sill depths, hence, none of the aforementioned assumptions are necessary and a classical grounding condition should be applied.

Additionally, we assume that icebergs do not interact with each other, that there is no limitation on the iceberg concentration in a grid box, and that the number of icebergs per grid box can be fractional.

2.2.5. Module Framework and Time Integration

The Eulerian iceberg module is a part of the MPIOM infrastructure and is implemented on an Arakawa-A grid (Arakawa & Lamb, 1977). It is forced by atmospheric and oceanic fields from MPIOM; therefore, vector quantities of atmospheric and oceanic forcing for the iceberg module are bilinearly interpolated from the Arakawa-C grid of the ocean model to the iceberg module's Arakawa-A grid on every time step. Scalar quantities do not require any interpolation, as they are defined on identical points. Iceberg drift velocities (Equation 2) are integrated on an Arakawa-A grid by an implicit Euler scheme (as in Savage, 2001) using the MPIOM time step. For the advection of iceberg concentrations (Equation 1), the iceberg velocities are averaged onto the velocity points of the Arakawa-C grid. The advection is performed using an explicit first order upwind scheme, as this ensures no artificial overshoots. The concentration changes due to melt and addition of icebergs (Equation 1) are calculated with an explicit scheme.

3. Simulated Iceberg Distribution and Sensitivity to Parameter Choices

In this chapter we evaluate the simulated iceberg distribution as well as the sensitivity of the iceberg module size classes representation to some parameter choices. We focus on model parameters that are introduced by our Eulerian model formulation. As the physical parameterizations are rather closely following the parameterizations used in for example, Martin and Adcroft (2010), we do not test their effect on the modeled iceberg distribution. The key quantity for our tests is the simulated distribution of the iceberg meltwater flux, as this is the climatically

Table 2
List of Sensitivity Experiments

Experiment	Experiment description	Number of size classes (N)
BIGG17	Modified iceberg sizes from Bigg et al. (1997)	17
LIN17	Linear iceberg height parameterization	17
EXP17	Exponential iceberg height parameterization	17
EXP09	Exponential iceberg height parameterization	9
EXP05	Exponential iceberg height parameterization	5
EXP03	Exponential iceberg height parameterization	3
EXP02	Exponential iceberg height parameterization	2

most relevant effect of icebergs as well as the simulated iceberg volume for evaluating our module's performance with regard to an available observational data set. We run a set of experiments focusing on the role of the prescribed relation between iceberg height and width (Figure 1). We also evaluate the difference in spatial meltwater flux distribution depending on the number of size classes.

We run the stand-alone MPIOM-Iceberg set-up in GR15 resolution (1.5° resolution with grid poles on south-eastern Greenland and the center of Antarctica) with 40 unevenly distributed levels. The ocean model in the standard set-up is forced with prescribed Ocean Model Intercomparison Project atmospheric forcing OMIP (Röske, 2001), which is a climatological forcing derived from reanalysis data but including daily variability. The diagnostic iceberg module is forced with observational estimates of present-day calving flux from Greenland and Antarctic ice sheets (Martin et al., 2022; Rignot et al., 2013). From a spun-up state for present-day climate without iceberg calving, the experiment was continued for 20 years with interactive icebergs. This length was sufficient for the iceberg distribution to reach a quasi-steady state. For the analysis the last 5 years of each simulation were used. Experiments are listed in Table 2. For the discretization of the iceberg size classes we choose an exponential increase of the volumes (Equation 20).

For the number of size classes we consider the following equation

$$N = 2^i + 1 \tag{21}$$

where $i = 0; 1; 2; 3; 4$ (or $N = 2; 3; 5; 9; 17$), whereby moving from i to $i + 1$ adds exactly one additional iceberg size class in between every neighboring pair.

We choose 17 ($N = 17$) iceberg size classes as a reference simulation based on the Equation 21. We have chosen here a rather large number of size classes to avoid potential artifacts due to a too low number of size classes. Later we determine the minimum number of classes required to get a good approximation of the results.

A constant iceberg height for the direct calving of big icebergs from ice shelves as given by BIGG input function Bigg et al. (1997) is probably a realistic assumption. Most of the melting of the icebergs occurs in the surface layer of the ocean and at the bottom of the iceberg. Therefore it is not a good assumption to keep the height of all big icebergs constant, although some of them are partly melted bigger icebergs. Additionally all big iceberg classes would generate an artificial peak in the vertical distribution of meltwater injection at this depth. To minimize this problem we choose the exponential relation between iceberg height and width (EXP; Equation 18) as it shows the most realistic vertical profiling of iceberg melt. Therefore, the reference experiment is called EXP17 (the number after the abbreviation corresponds to the number of size classes N).

We focus our validation on the southern hemisphere, where our prescribed forcing represents the amount of iceberg calving. Due to the lack of true iceberg calving flux estimates in the northern hemisphere, we had used the total mass loss rate of the Greenland sheet, which represents both solid and liquid discharge from the ice sheet, as forcing for our iceberg module. As a consequence, our forcing and thus our results overestimate the presence of icebergs.

Figure 2 shows both simulated iceberg mass per area and the observational estimate averaged over the years 1994–2021 (Tournadre, 2022; Tournadre et al., 2016) for the southern hemisphere. The simulated pattern is quite

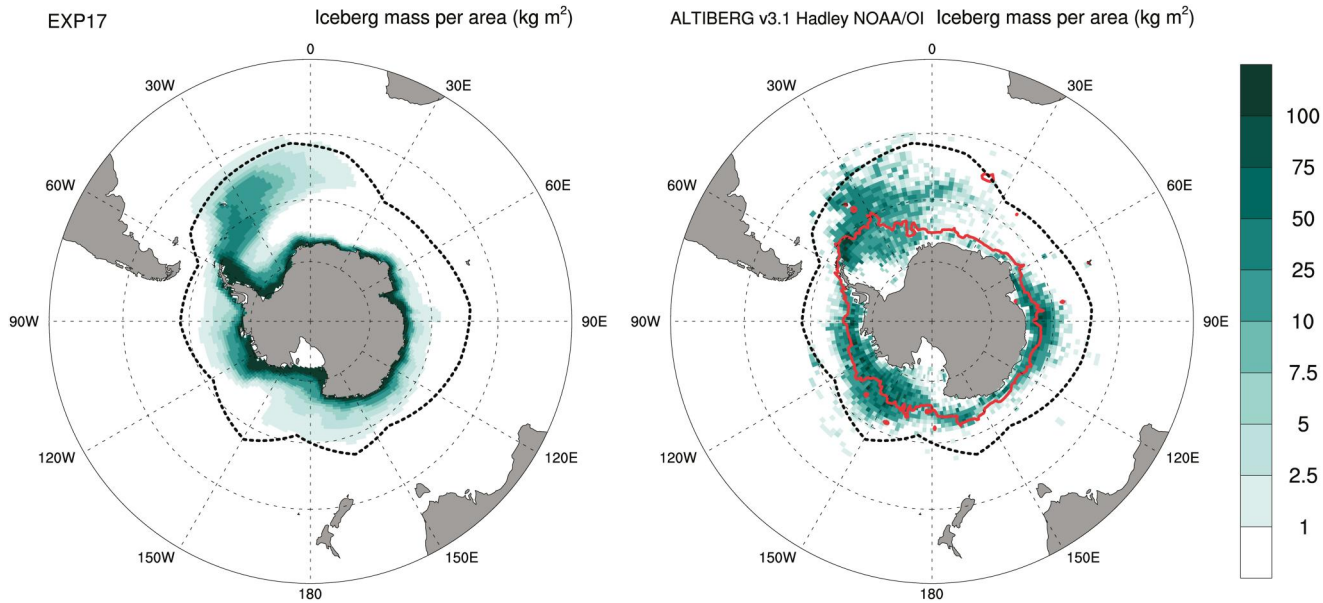

Figure 2. Mean February iceberg mass per area (kg m^{-2}) for the simulation with $N = 17$ iceberg size classes (EXP17, left) and observed (1992–2021, right) in the Southern Hemisphere (Tournadre, 2022; Tournadre et al., 2016). The observations cover icebergs smaller than 3 km length and are only given for ice free ocean areas. Therefore the maximal February sea ice extent (Hurrell et al., 2008; Shea et al., 2020) for the period 1992 to 2021 is indicated by a red line. The black dashed lines denote the observed iceberg extent (Jongma et al., 2009; Wagner et al., 2017). Note the logarithmic scale of the colorbar.

realistic, but the observations seem to indicate slightly higher values far away from the source regions. This seems to indicate a slight overestimation of the melting. This could either be caused by too warm ocean temperatures or by the choice of our size classes, which do not include giant icebergs.

The observed iceberg extent from Wagner et al. (2017), Jongma et al. (2009) are shown in Figures 2, 3, and A1 in dashed line. Additionally, Figure 3 shows one isoline of the total iceberg concentration (summed up over all iceberg classes, solid line) corresponding to one iceberg per box with 100 km side length.

The distribution of the meltwater flux from icebergs for this experiment is shown in Figure 3 (top). As expected, the highest values are simulated close to the calving sites. The module shows a too large iceberg extension southeast of Greenland. This can be explained by the too zonal path of the simulated North Atlantic current and the lack of a northwest corner known from observations (Lazier, 1994). This leads to too cold temperatures in the ocean model, which results in an underestimation of the iceberg melt in this region.

For comparison we show the iceberg meltwater flux from Martin and Adcroft (2010), Merino et al. (2016) in Figure A1. The simulated pattern in the other two models is more confined to the coast of Antarctica than the results from our model. Keeping in mind that our model shows an underestimation of the iceberg mass far away from Antarctica, this could be an indication that our model is more realistic in this respect. However, the results are rather sensitive to the modeled temperature and sea ice distribution and the prescribed size distribution of the iceberg calving flux.

The relation between iceberg volume and iceberg height is a rather uncertain parameter in our module. Therefore we have tested in addition to our exponential approach (EXP17) two other relationships, all of them adapting somehow to the BIGG input function.

The first relation (BIGG17) is directly derived from Bigg et al. (1997). It is characterized by equal height and width for iceberg heights of up to 360 m and a constant height of 360 m for larger icebergs. The second alternative relation (LIN17) uses a linear relation between iceberg height and width:

$$H(n) = a + bW(n) \tag{22}$$

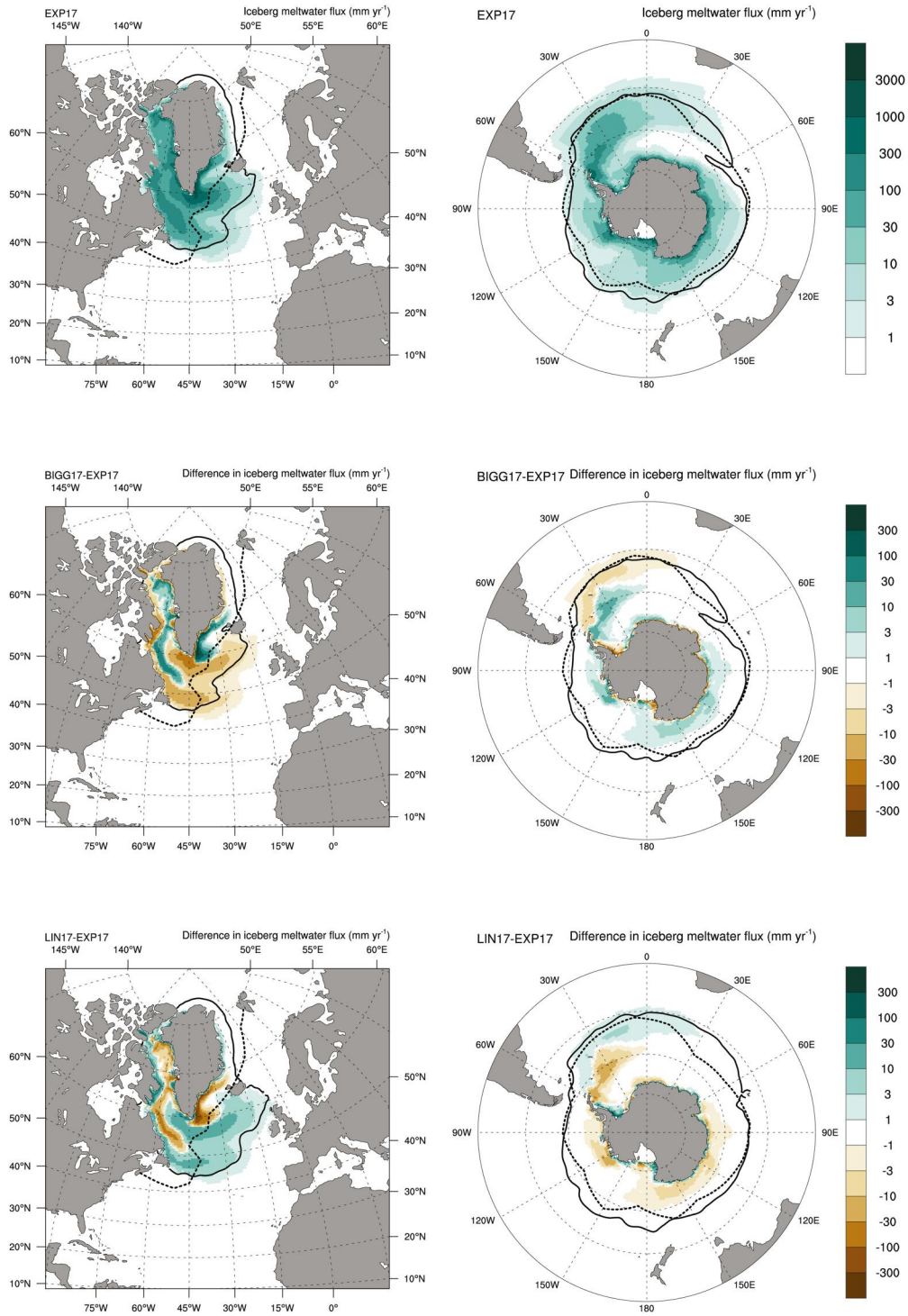

Figure 3. Annual mean iceberg meltwater flux (mm yr^{-1}) for the exponential iceberg height parameterization with $N = 17$ (EXP17, top). Total prescribed Greenland calving flux is 576 Gt yr^{-1} (18 mSv, Martin et al., 2022). Total calving flux for Antarctica is 1,089 Gt yr^{-1} (35 mSv, Rignot et al., 2013). Difference in iceberg meltwater flux between the parameterizations based on the classical input function and the exponential iceberg height parameterization (BIGG17-EXP17, middle), and between linear and exponential iceberg height parameterizations (LIN17-EXP17, bottom). Black solid lines indicate the simulated total iceberg concentration of 10^{-10} m^{-2} in EXP17 (top), BIGG17 (middle), and LIN17 (bottom). Black dashed lines denote the observed iceberg extent (Jongma et al., 2009; Wagner et al., 2017). Note the logarithmic scale of the colorbar.

where a and b are calculated from the given volumes of the smallest and the biggest iceberg size classes, $W_{\min}$ and $H_{\max}$. All relationships between height and width are shown in Figure 1 and listed in Table 2.

The effect of different assumptions about the relation between iceberg width and height is shown in the two lower panels in Figure 3. BIGG17 leads to iceberg melt closer to the calving sites. This can be explained by the reduced drift velocity due to the larger iceberg height (see iceberg heights in BIGG17 and EXP17 in Figure 1), which reduces the relative contribution of wind forcing to the iceberg drift in relation to the contribution from subsurface ocean layers. The effect of the linear approach LIN17 results in the opposite effect. However, the uncertainty to the prescribed dependence of height versus width is relatively small compared to the total meltwater flux. The effect on the simulated iceberg extent is rather small as well. Based on this and the fact that the exponential approach leads to a more gradual vertical distribution of the meltwater between the ocean surface and the depth corresponding to the bottom of the biggest iceberg, we consider the exponential approach as a reasonable choice for the representation of the iceberg height.

Next, we evaluate how many iceberg size classes are sufficient to realistically resolve the distribution of iceberg meltwater flux. As the computational cost strongly increases with the number of size classes, a relatively low number of classes is desirable. For this we ran sensitivity experiments using the exponential iceberg height parameterization in the same model configuration as above for a set of experiments differing in the number of iceberg size classes, defined as in Equation 21 for $i = 0; 1; 2; 3; 4$ or $N = 2; 3; 5; 9; 17$.

The sensitivity experiments show that the lower the number of iceberg size classes in the module the more intense iceberg meltwater flux is simulated close to the calving sites and the less icebergs melt in remote areas (see for differences between $N = 2$ and $N = 17$, $N = 5$ and $N = 17$, and $N = 9$ and $N = 17$ in Figure 4). The difference between 2 and 17 iceberg size classes is rather high, whereas for 5 or more iceberg size classes, the differences compared to the use of 17 iceberg classes are rather small. Choosing the number of size classes between 5 and 17 does not result in considerable changes of the calculated iceberg meltwater flux. Thus, already 5 classes yield a rather good approximation, which helps to keep the computational effort low. Using $N = 2$ iceberg size classes in MPIOM GR15 costs approx. 4% of the total computations time, $N = 5$ iceberg size classes nearly 8%, and $N = 17$ costs 24% (Table A1). The extra computational cost of the iceberg module with $N = 5$ in coarser GR30 configuration is about 5%. Iceberg characteristics for $N = 5$ are presented in the Table 3. It should be noted that five iceberg size classes should be sufficient for long term climate studies when the fate of individual icebergs is not of the interest. For studies focusing on the task of evaluating the number of icebergs in North Atlantic for ship navigation, the model should include more size classes. Moreover, the Lagrangian approach is likely to be more accurate, especially if the position of every individual iceberg matters.

4. Effect of Iceberg Calving and Freshwater Hosing

In this section we analyze a set of idealized multi-millennial experiments that are intended to shed light on the importance of iceberg calving in comparison to two different types of freshwater hosing and are intended as an argument to include interactive iceberg modules in long-term climate change simulations, for example, deglacial simulations (Ivanovic et al., 2016; Kapsch et al., 2022), especially as our formulation of an iceberg model allows to do so at rather moderate computational cost.

The design of the study is highly idealized and does not aim at any specific time slice but rather at better comparability with previous water hosing studies. This follows a tradition of papers investigating the AMOC response to meltwater forcing (e.g., Gregory et al., 2003) as a tool to investigate the stability of present days climate and to test whether multiple steady states of the AMOC exist. One major goal of these experiments is to demonstrate the importance of including interactive icebergs in this type of simulations. We compare the effect of iceberg calving from Hudson Strait with the effect of direct freshwater hosing, either added as a point source or distributed over a latitude belt in the North Atlantic. Typical experimental designs are hosing simulations (of a few centuries) with a fixed forcing followed by some time without forcing to analyze the recovery (e.g., Levine & Bigg, 2008; Wiersma & Jongma, 2010). Here we are aiming at comparing threshold values for the different types of prescribed freshwater hosing/iceberg calving. Rather than running a set of experiments with different hosing rates for each of the forcing types, we performed simulations with slowly varying forcing yielding an approximation of a hysteresis curve with the advantage that the delayed AMOC effect due to iceberg melting is small, as the AMOC response is always close to the equilibrium response like

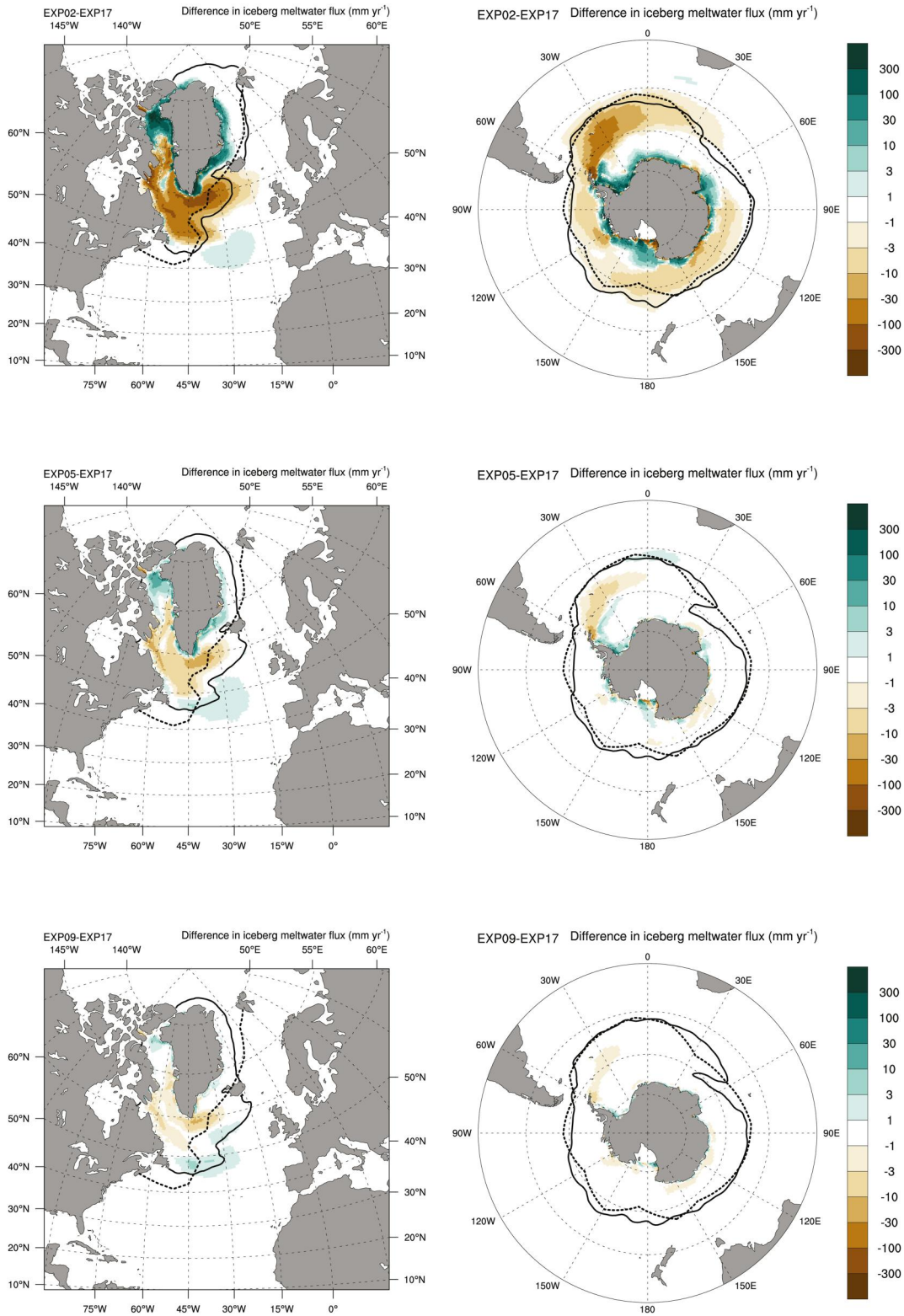

Figure 4. Difference in simulated iceberg meltwater flux (mm yr^{-1}) between $N = 2$ and $N = 17$ (EXP02-EXP17, top); $N = 5$ and $N = 17$ (EXP05-EXP17, middle); $N = 9$ and $N = 17$ (EXP09-EXP17, bottom). Total prescribed Greenland calving flux is 576 Gt yr^{-1} (18 mSv, Martin et al., 2022). Total calving flux for Antarctica is 1,089 Gt yr^{-1} (35 mSv, Rignot et al., 2013) Black solid lines indicate the simulated total iceberg concentration of 10^{-10} m^{-2} in EXP17 (top), BIGG17 (middle), and LIN17 (bottom). Black dashed lines denote the observed iceberg extent (Jongma et al., 2009; Wagner et al., 2017). Note the logarithmic scale of the colorbar.

Table 3
Iceberg Sizes in the Eulerian Iceberg Module With the Number of Size Classes N = *5*

Class	Length (m)	Width (m)	Keel (m)	Sail (m)	Fraction (%)
1	32.2	21.5	18.5	2.3	0.0
2	78.5	52.4	43.3	5.5	13.0
3	195.6	130.4	97.1	12.3	31.8
4	513.4	342.2	196.1	24.8	43.6
5	1,544.9	1,029.9	301.3	38.1	11.6

in Mikolajewicz and Maier-Reimer (1994) and Rahmstorf (1996). To the authors knowledge, this is the first time a hysteresis experiment to study AMOC sensitivity is carried out with an interactive iceberg module. We show that the hosing induced climate response has a strong effect on the pattern of iceberg melt, which indicates that prescribing a fixed melt pattern is not an adequate solution, and discuss the effect of the latent heat effect.

4.1. Experimental Design

4.1.1. Spin-Up

The spin-up was branched off at 1840 CE from a long transient deglacial simulation with prescribed ice sheets from GLAC-1D (Tarasov et al., 2012) described in Kapsch et al. (2020) and integrated for 4,500 years with constant forcing corresponding to conditions equivalent to 1840 CE. Atmospheric greenhouse gas concentrations were prescribed from Köhler et al. (2017). Insolation was calculated following Berger and Loutre (1991). All experiments described in the following were started from the model state reached at the end of the spin-up. Except for the iceberg module, the model is identical to model version P2 used in Kapsch et al. (2020).

Due to the placement of one model grid pole of the ocean grid on south-east Greenland, this coarse resolution MPI-ESM-CR set-up with 3° resolution yields a higher spatial resolution in the North Atlantic subpolar gyre (between approx. 40 km at the coast of East Greenland and 150 km at the coast of Britain). The ocean grid used here is coarser than the one used in Section 3, which is motivated by the turnaround required for multi-millennial simulations. It is identical to the one used in simulations of the last deglaciation Kapsch et al. (2022).

4.1.2. Design of Hosing Experiments

The idealized hosing experiments conducted for this study are summarized in Table 4. In experiment IB, hosing is treated as iceberg calving using our new interactive Eulerian iceberg module to determine iceberg drift and melt. The input location is in the Labrador Sea in front of Hudson Strait (Figure 5). In a sensitivity experiment (IBnoLH), the latent heat of icebergs is set to 0. This experiment aims at separating the effects of meltwater input and upper ocean cooling due to iceberg melt.

In two other experiments, hosing is treated as direct injection of liquid freshwater. In a classical freshwater point source hosing experiment FWPS, the freshwater is released in the same location as in both iceberg experiments (similar to, e.g. Maier-Reimer & Mikolajewicz, 1989; Schiller et al., 1997). In the freshwater North Atlantic experiment FWNA, the freshwater release is uniformly distributed over the northern North Atlantic between 50° and 70°N (like in, e.g. Kageyama et al., 2013; Otto-Bliesner & Brady, 2010; Stouffer et al., 2006). Figure 5 shows the hosing locations for all experiments.

In an additional experiment with icebergs CTRL, the feedback of the icebergs on climate has been suppressed. Thus, the simulated climate in this experiment is not affected by the hosing, the icebergs are purely diagnostic. This experiment serves as control experiment for the other runs and permits investigation of the effect of hosing-induced ocean climate changes on iceberg distribution and melting as well as to quantify the residual climate drift in the model.

Table 4
List of Pre-Industrial Hosing Experiments

Experiment	Experiment description
IB	Iceberg experiment
IBnoLH	Iceberg experiment with no latent heat
FWPS	Freshwater point source experiment
FWNA	Freshwater North Atlantic experiment with hosing between 50° and 70°N
CTRL	Control experiment with purely diagnostic icebergs

In all experiments, the prescribed input-hosing-rate (hereafter referred to as input rate) linearly increases from 0 to 0.35 Sv in the first 3,500 years of each experiment and decreases afterward linearly to 0 Sv within the next 3,500 years. The rather slow rate of change in input rate of 0.1 Sv in 1,000 years results in a reasonable approximation of the steady-state response of the climate system. This experimental design aims at determining threshold-hosing-rates for an AMOC transition from a strong to a weak mode (and vice versa) for the different types of hosing. After the prescribed input rate has reached zero again, all experiments are continued for 500 years without any perturbation to allow some equilibration.

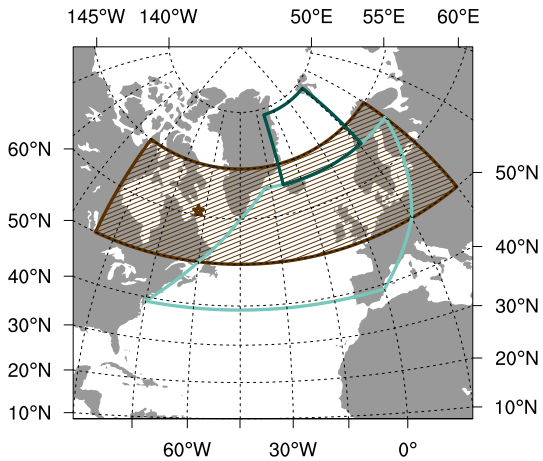

Figure 5. Location of hosing sites: brown star denotes the location in IB, IBnoLH, and FWPS; brown box in FWNA. Light green and dark green boxes denote locations of the northern North Atlantic and Nordic Seas basins, respectively.

4.2. Climate of Reference Simulation

First, some key quantities describing the climate of the unperturbed reference experiment CTRL are presented. Due to the lack of observations from this period, we are comparing our simulation with modern observations, but we have tried to use periods as early as possible to minimize the influence of anthropogenic climate change on the observational climatology. Depending on the availability of data, this lead to different optimal time periods for different quantities.

This serves as a reference for the discussion of the hosing effects below. The analysis focuses on the climate of the northern Atlantic and the Nordic Seas, as this is the most relevant region for North Atlantic deep water (NADW) formation and thus variations in the AMOC. We are using years 200–399 for this analysis. Therefore, SST and sea surface salinity (SSS) fields, winter mixed layer depth, and summer and winter sea-ice extent are presented for this region.

In the reference experiment CTRL (Figure 6; first row), the vast majority of NADW forms in the Nordic Seas where the seasonal maximum of the mixed layer depth reaches more than 3,000 m. Mixed layer depth is defined here using a density criterion of 0.125 kg m^{-3}. This quantity is an indicator of active deep water formation. Some deep water formation also takes place in the Labrador Sea, south of Greenland, and in the Irminger Sea, south-east of Greenland, with a seasonal maximum of the mixed layer depth of 2,000 m. The observational estimate from Locarnini et al. (2018) and Zweng et al. (2019) shows similar patterns, but much shallower values (Figure 6; second row). The general pattern of SST and SSS are reproduced by the model, but in the North Atlantic centered around 40° and 50°N and 40° to 20°W a cold and fresh bias is visible, a pattern quite typical for coarse resolution climate models (see e.g. IPCC AR5 WG1, Flato et al. (2013) Chapter 9, Figure 9.2, or Jungclaus et al. (2013)).

The simulated summer and winter sea ice extents are quite realistic (Hurrell et al., 2008; Shea et al., 2020). The slightly overestimated winter sea ice extent in the Nordic Seas could be a consequence of comparing a simulation with preindustrial forcing with observations during a period with higher greenhouse gas concentrations and somewhat warmer climate.

The maximum strength of the AMOC (below 500 m) at 26°N is 17.8 Sv (see Figure A5). For other 200 year periods of the CTRL values between 16.7 and 18.8 Sv are simulated. Whereas the overturning strength fits very well with estimates from for example, the RAPID array (17.0 ± 4.4 Sv from April 2004 to February 2017 in Frajka-Williams et al. (2019)), the simulated implied Atlantic ocean heat transport at 26°N over the reference period is 0.81 PW. For other 200 yr periods values between 0.77 and 0.84 PW are simulated. This is somewhat lower than the observation based heat transport estimates (e.g., 1.25 PW from April 2004 to October 2012, McCarthy et al., 2015 or 1.15 PW over the period 2009–2016, Bryden et al., 2020).

In general, the model produces a reasonable realistic climate. The biases are consistent with the biases typical for higher-resolution versions MPI-ESM model (e.g., Jungclaus et al., 2013; Mauritsen et al., 2019).

To put the AMOC sensitivity of MPI-ESM into context to other models, we additionally performed a hosing experiment as outlined in the model intercomparison experiment described in Stouffer et al. (2006). The response of our MPI-ESM set-up (see Figure A3) lies well within the range spanned by other models, and even belongs to the more sensitive models.

4.3. Effect of Hosing

The main focus of the experimental set up is to understand the effect of the type of hosing (icebergs, freshwater point source and latitude belt) on the sensitivity of the AMOC. All the displayed spatial distributions of properties in this section correspond to averages over 200 years. Timeseries display 100 running means.

In the beginning of the hosing experiments, all runs show a qualitatively similar response, although with some differences in their strength. The prescribed injection of icebergs/freshwater reduces the surface salinity in the

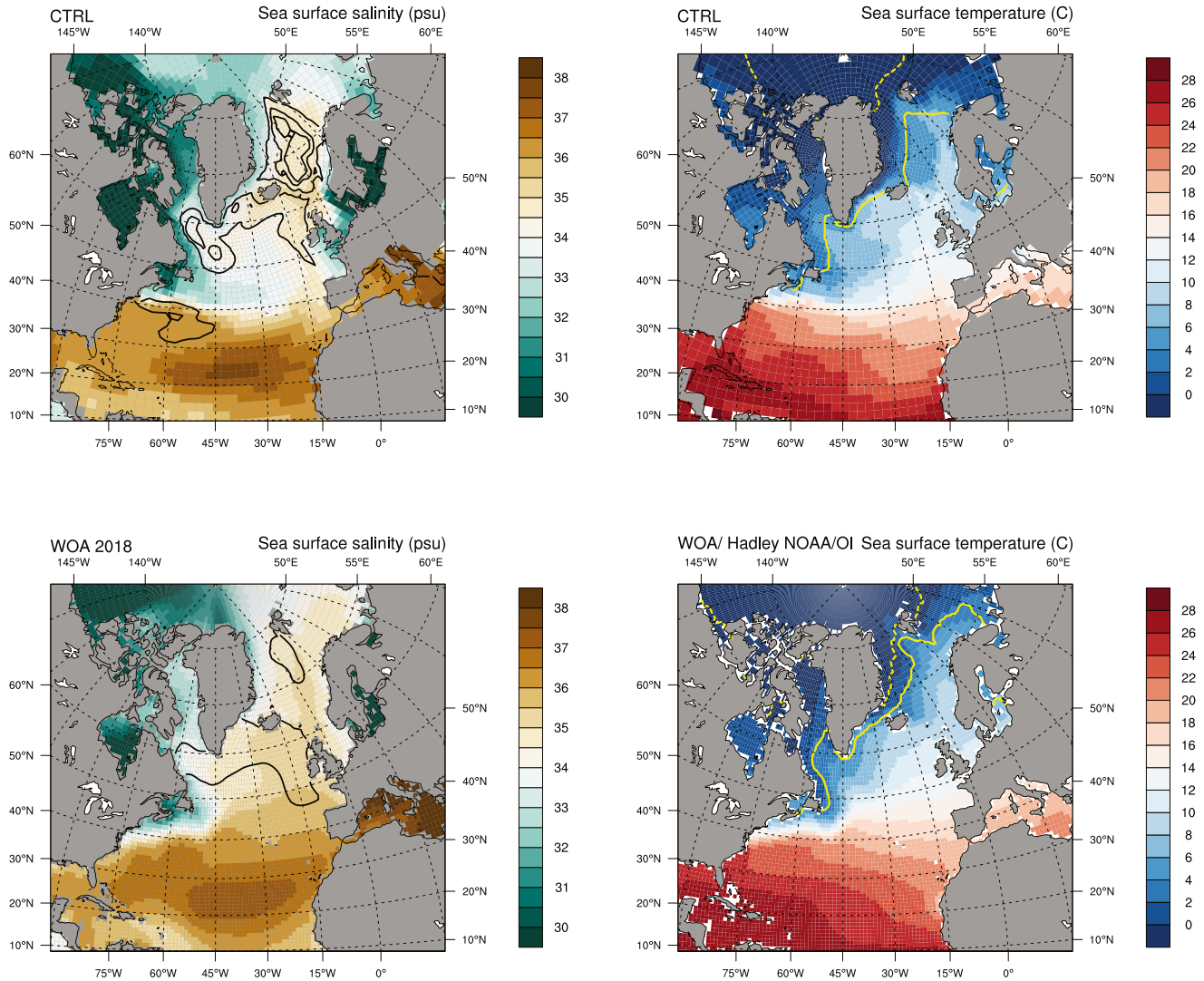

Figure 6. Sea surface salinity (SSS) (psu) and the seasonal maximum of mixed layer depth (m; isolines denote values of 500, 1,500, 2,500, and 3,500 m; left), and Sea surface temperature (SST) (°C; right) and winter (yellow solid line) and summer (yellow dashed line) sea-ice concentration of 15%. First row shows simulated data and the second row shows observational data. Observational SSS and SST are averaged over 1985–1994 (Locarnini et al., 2018; Zweng et al., 2019). Observational mixed layer depth is averaged over period 1981–2010 (Locarnini et al., 2018; Zweng et al., 2019). Observational sea-ice concentration is averaged over period 1951–1990 (Hurrell et al., 2008; Shea et al., 2020).

North Atlantic and the Nordic Seas (Figure 7b). This reduces deep convection in the Nordic Seas (indicated by the integral over the seasonal maximal mixed layer depth, see Figure 7c) and thus NADW formation and leads to a weakening of the AMOC (see Figure 7d). Northward heat transport in the North Atlantic is reduced as well (see Figure 7e).

For input rates smaller than 0.046 Sv, the system response is an almost linear function of the input rate for all experiments (Figures 7 and 8). The weakening of the NADW results in a linear decrease of the AMOC strength from nearly 18 to 16 Sv, which causes a decrease of almost 10% in the northward heat transport across the northern North Atlantic (see Figures 7d and 7e). The latter leads to a cooling in North Atlantic SSTs. The reduced mixed layer depth reduces the effective heat capacity of the surface ocean in winter, thus further amplifying the surface cooling (Figure 7f) and the extension of sea-ice (not shown).

Further increase of the hosing strength brings the system close to a state, where the system response becomes highly nonlinear. This can be seen by the abrupt drops of the AMOC strength (typically from around 14 Sv to about 8 Sv). The hosing rate at which this abrupt change starts is termed threshold value in the following.

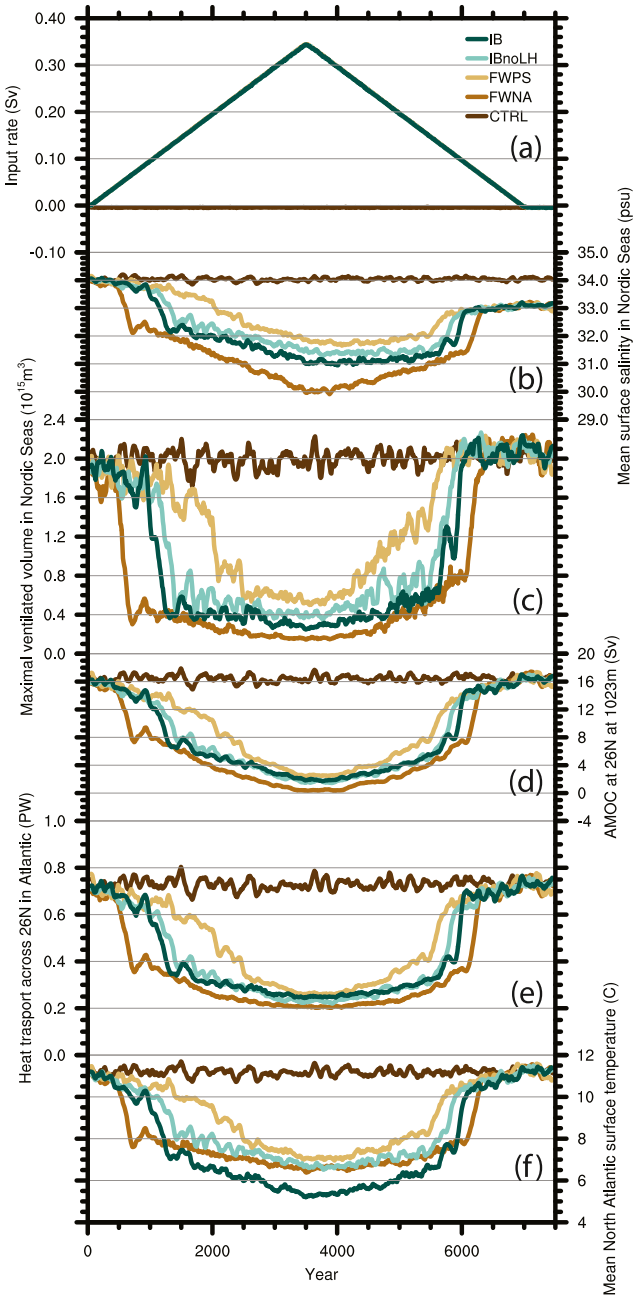

Figure 7. 100-years running mean of (a) input rate (Sv); (b) mean sea surface salinity in the Nordic Seas (psu); (c) maximal seasonal ventilated volume in the Nordic Seas (m^3); (d) Atlantic meridional overturning circulation strength at 26°N at 1023m (Sv); (e) northward Atlantic heat transport across 26°N (PW); (f) mean Sea surface temperature in the northern North Atlantic (°C). The northern North Atlantic and the Nordic Seas basins are presented in Figure 5. Dark brown line corresponds to CTRL, light brown to FWPS, medium brown to FWNA, dark green to IB, and light green to IBnoLH.

To allow for a better interpretation of the hysteresis behavior, the AMOC strength is also shown as a function of the input rate in Figure 8, similarly to classical hosing studies (e.g., Gregory et al., 2003; Mikolajewicz & Maier-Reimer, 1994; Rahmstorf, 1996, 2002; Stommel, 1961).

In the experiment with interactive icebergs IB the threshold value lies at approx. 0.094 Sv. Latitude belt freshwater hosing FWNA is more effective to reduce the AMOC with a threshold of 0.050 Sv. The AMOC is less sensitive against point source forcing in the Labrador Sea FWPS as indicated by a threshold of 0.133 Sv. In this experiment the switch toward the weak AMOC mode occurs in a series of steps, each of them associated with an abrupt weakening or suppression of deep water formation in different regions (first in the Labrador Sea, the north-western North Atlantic including Irminger Sea and Nordic Seas, second and third in the Nordic Seas predominantly). After the collapse, the AMOC drops to approx. 6 Sv. Further increase of the hosing has only small effect on the AMOC, as it never drops below 5 Sv. For the collapsed AMOC, the NADW cell is rather shallow for strong hosing, indicating the formation of intermediate water rather than deep water (not shown). After decreasing the prescribed hosing rate again, the climate approaches in all hosing experiments the climate of the control simulation CTRL, except that the salinity is approx. 0.95 psu lower due to the addition of freshwater. Atlantic overturning strength and northward heat transport as well as the temperature distribution are in all simulations very similar to the initial values.

To test how close the threshold values estimated from our experiments are to the real threshold values obtained by simulations with infinitesimal slow changes in the input rates, an additional experiment with interactive iceberg was performed, where the rate of change of the prescribed iceberg input was halved, otherwise the experiment is identical to experiment IB. The result (see Figure A4 in Appendix A) indicates that a halving of the rate of change of input rates has only a small effect on the estimated threshold value, which is an indication that our experimental setup seems to give a reasonable approximation of the steady state thresholds.

To investigate in more detail the causes for the strong dependence of the threshold value, we focus on a hosing rate when the AMOC is in the strong mode in all experiments and the system response is still rather linear. We chose a time slice corresponding to a mean input rate of 0.04 Sv.

At this time slice, the calculated meltwater flux distribution from experiment IB as well as the iceberg volume is shown in Figure 9. The meltwater flux is maximal close to the imposed calving site off the Hudson Strait where also the iceberg volume is maximal. The melting decreases toward east and reaches maximal values for each longitude between 40° and 60°N. The simulated melt in relation to the available iceberg volume at a location shows that the melt in the northern edge of the distribution is somewhat stronger than in the southern edge. From the temperature distribution one would expect stronger iceberg melt in the south than in the north of the iceberg plume. This at first counter-intuitive distribution can be explained by the differences in iceberg size distribution. In the north, small icebergs with a large surface area relative to the volume dominate. In the south, more large icebergs with a relatively small surface area in relation to the volume prevail. The reason for this are differences in iceberg drift velocity and direction for small and large icebergs. The drift of small icebergs is largely controlled by the wind, whereas the drift of the large icebergs is dominated by the effect of ocean currents. Therefore, small icebergs have a larger drift velocity and follow a more

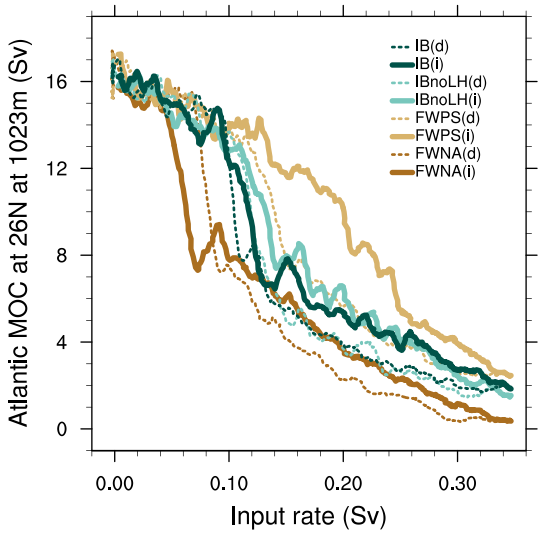

Figure 8. Atlantic meridional overturning circulation strength at 1,023 m at 26°N (Sv) versus input rate (Sv). Solid lines (i) depict the first part of experiments when input rate increases; dashed lines (d) correspond to the second part of experiments when input rate decreases.

northerly route than big icebergs (Figure 10). Together with the stronger effect of wave erosion, this difference in iceberg size outweighs the temperature effect.

The changes in SSS for the three experiments at this time slice (see Figure 11) show a clear freshening of the northern North Atlantic. In the point source experiments (IB, FWPS), the freshening has a clear maximum in the southern margin of the Labrador Sea, downstream of the release site. The freshwater is advected across the North Atlantic. A southward shift of the water mass boundary between the subpolar and subtropical gyres further amplifies the negative salinity anomaly. Following the path of the subpolar gyre, the water spreads northward before a part penetrates into the Nordic Seas, while another part spreads westward south of the sills. There is a clearly visible southward spread of the fresher water in the Canary current, similar to the results from Swingedouw et al. (2015).

In experiment FWNA, with uniform input rates across the North Atlantic, the freshening is strongest at the European coast, the North and Baltic Seas and the Norwegian current. This enhanced transport of the freshening signal to the Nordic Seas, the key region for the formation of NADW, explains the rather strong response in the FWNA experiment. In experiment FWPS, the freshening in the Norwegian current is weakest, explaining the rather high stability of the system against this type of hosing. Experiment IB with interactive icebergs is somewhere in between the two freshwater hosing experiments, matching with the aforementioned distribution of the meltwater release from icebergs (see Figure 9). The pattern of change in SST somewhat resembles the changes in SSS except for the sea-ice covered regions, where the SST decrease is limited by the freezing point. The Barents Sea and the eastern Greenland Sea even show a slight warming signal, which is caused by a reduction of the cooling of inflowing subsurface waters from the North Atlantic south of the sills, due to reduced surface salinity. As consequence the relative warm subsurface waters now reach the surface in the Barents Sea and Greenland Sea.

There is a distinct effect of the simulated climate on the simulated pattern of iceberg meltwater flux. This is illustrated for the time slice with 0.2 Sv prescribed input rate (see Figure 12), where the AMOC is already collapsed in experiment IB. SST in the northern North Atlantic has substantially cooled and sea-ice has expanded. The simulated meltwater flux is the largest in the immediate vicinity of the hosing site off the Hudson Strait and

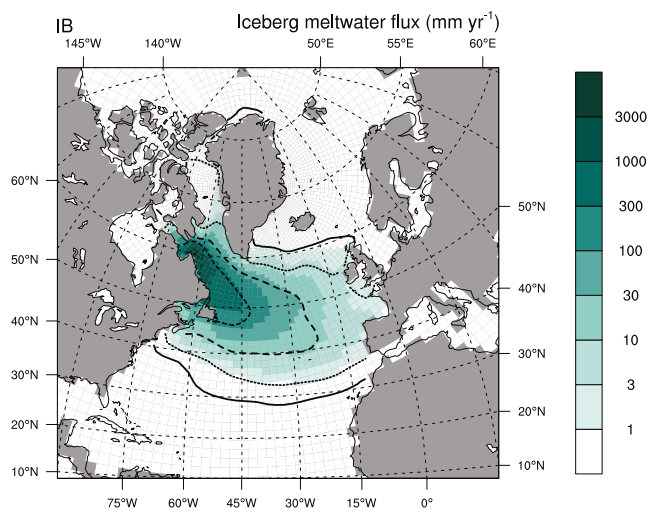

Figure 9. Iceberg meltwater flux (mm yr^{-1}) before the Atlantic meridional overturning circulation collapse at 0.04 Sv. Isolines denote the ratio between iceberg volume and grid area in a grid box (solid 10^{-3} m, dotted 10^{-2} m, long-dashed 10^{-1} m, short-dashed 1 m).

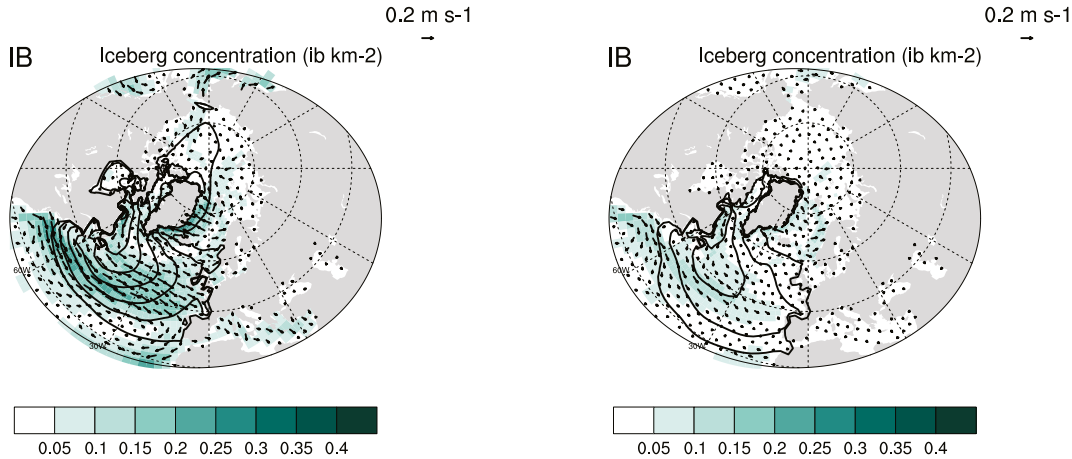

Figure 10. Simulated velocities (vectors) for the smallest (left, $n = 1$) and the biggest (right, $n = 5$) iceberg size classes (m s^{-1}) in Northern hemisphere at an input rate of 0.04 Sv. Color shades denote velocity magnitudes (m s^{-1}). Isolines denote iceberg concentrations (ib m^{-2}). The lowest (southernmost) concentration corresponds to 10^{-12} ib m^{-2}. Contour interval is logarithmic, with a factor of 10 between neighboring isolines.

extends all across the North Atlantic reaching the European coast. Comparison of this pattern to the simulation with purely diagnostic icebergs (Figure 12), which shows the effect of the climate changes on iceberg melting, indicates that the surface and subsurface cooling due to the collapsed AMOC and heat consumption due to melting icebergs strongly enhances the lifetime of icebergs, reducing melt especially in the Labrador Sea. The meltwater release in the northeast Atlantic, especially close to the European coast, is enhanced by approximately one order of magnitude relative to CTRL. The simulated iceberg concentrations increase by a factor of approximately six (for big icebergs) to 30 (for small icebergs; not shown). Given the large sensitivity of the AMOC response to the location of meltwater input, this effect is clearly relevant, especially for phases of AMOC recovery. This also demonstrates the necessity to interactively couple an iceberg component into the ocean model rather than using a fixed melt pattern, which would be the simplest and cheapest method to consider the effect of icebergs.

However, the changes in AMOC are not the only effect of icebergs on SST. When icebergs melt, heat is required, leading to a cooling of the upper ocean. The surface ocean cools and sea-ice cover extends further. This effect is demonstrated by comparing the standard IB experiment with a sensitivity experiment where the latent heat of icebergs was set to zero (IBnoLH, Figure 12b). The upper ocean cooling due to the heat required to melt icebergs contributes substantially to the increase of iceberg lifetime and to the increase in iceberg presence and melt in the Northeast Atlantic. This also causes a decrease of surface iceberg meltwater flux and a corresponding increase of subsurface melt (not shown).

The upper ocean cooling partly compensates for the density effect due to the meltwater induced freshening, thus leading to a higher AMOC stability. But the cooling also reduces the melt of icebergs, allowing them to travel further to the east, enhancing the weakening of the AMOC. The effects of the upper ocean cooling and the longer iceberg lifetime cancel to some degree, leading to a slightly lower sensitivity of the AMOC to the input rate (by approx. 0.02 Sv, see Figures 7 and 8).

In contrast to results from previous studies (Jongma et al., 2009; Levine & Bigg, 2008; Wiersma & Jongma, 2010), comparing the effects of iceberg calving versus freshwater hosing, our results are less sensitive to the latent heat effect of icebergs. Jongma et al. (2013) found in hosing experiments using an Earth model of intermediate complexity under Last Glacial Maximum (LGM) conditions that iceberg latent heat substantially enhanced the sensitivity of the AMOC against iceberg discharges. The authors also found a stronger AMOC sensitivity for freshwater hosing in the Ruddiman belt (Ruddiman, 1977) compared to iceberg hosing in the southwest Labrador Sea, which fits to our results. Levine and Bigg (2008) found in a set of simulations under LGM conditions a stronger AMOC sensitivity against point source freshwater hosing compared to iceberg discharge. The discrepancy could be due to the LGM background climate and to the fact that many of their calved icebergs became grounded close to the hosing site and did not travel onto the open Atlantic. The latter effect was excluded from our experimental setup. On the other hand, Wiersma and Jongma (2010) found a higher climate

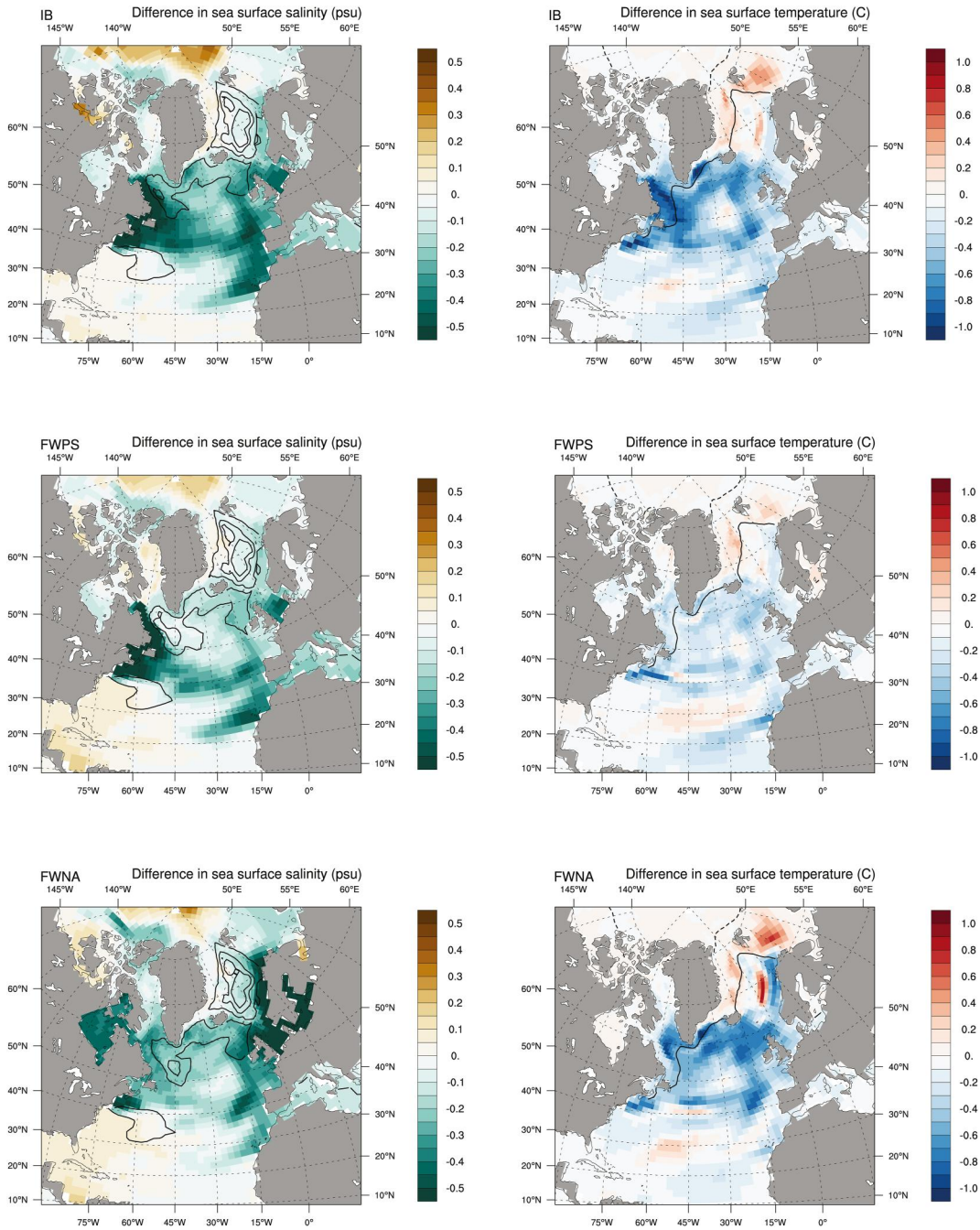

Figure 11. Difference in sea surface salinity (psu; left) overlayed by maximal mixed layer depth (m; isolines denote values of 500, 1,500, 2,500, and 3,500 m); and sea surface temperature (°C; right) overlayed by sea-ice extent (black lines; winter (solid) and summer (dashed) sea-ice concentration of 15% in hosing experiment) between hosing (IB (top); FWPS (middle); and FWNA (bottom)) and CTRL before the Atlantic meridional overturning circulation collapse.

sensitivity for iceberg discharge compared to point source freshwater hosing under early Holocene boundary conditions. The prescribed disturbance was, however, rather short (5 years). Nevertheless, this points into the same direction as the results from our longterm simulations.

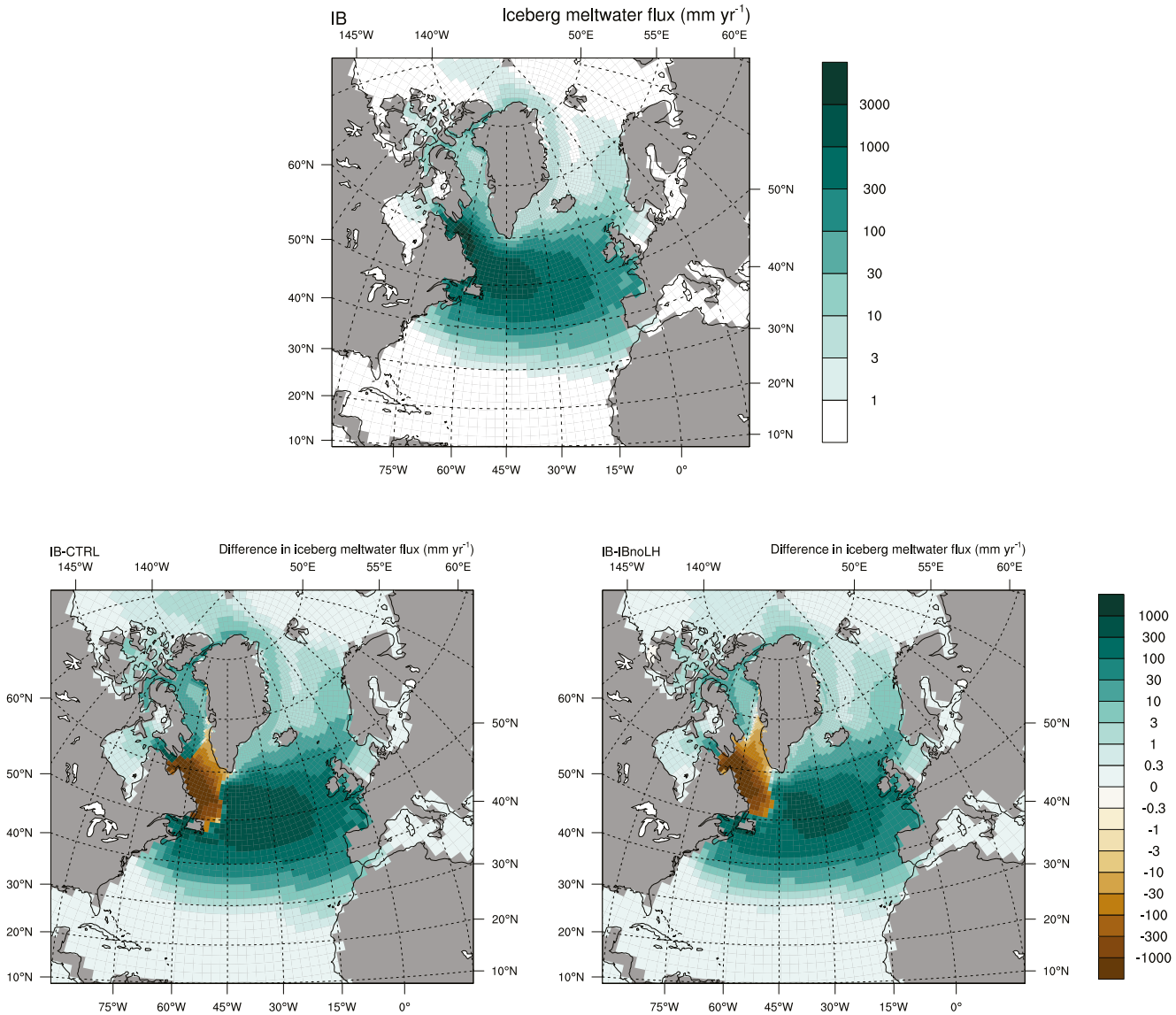

Figure 12. Iceberg meltwater flux at 0.2 Sv (mm yr^{-1}) in IB (top). Difference in iceberg meltwater flux at 0.2 Sv between IB and CTRL (mm yr^{-1}, left) and IB and IBnoLH (mm yr^{-1}, right).

5. Summary and Outlook

In this work, we have formulated a new Eulerian iceberg module. Rather than tracking individual icebergs (or groups of icebergs), icebergs are described as concentrations of predefined size classes. For the calculation of iceberg melt and velocity, standard equations, as used in Lagrangian iceberg modules, are used.

This iceberg module is specifically designed for the use in long-term climate simulations with model systems that include an interactive ice sheet component. As the computational cost does not depend on the number of icebergs present in the system, our approach has great advantages for climates in which many icebergs originate from many different sites, for example, during glacial climates. With our parameter choices our Eulerian iceberg module costs approx. 8% of the CPU time of the ocean component of MPI-ESM. As in many climate models, the atmospheric component is the more costly one, CPU costs should no longer be a valid argument for not using an interactive iceberg component. Here we expect the Eulerian approach to be computationally more efficient than the widely used Lagrangian approach. For simulations with few source

locations the Lagrangian approach combined with some grouping that is likely to be computationally cheaper. The simulated iceberg meltwater flux distribution is not very sensitive to the chosen number of iceberg size classes and the prescribed relation between iceberg height and width. Simulations for present day show that the simulated iceberg distributions are plausible compared to available iceberg data and other models.

We investigated the effect of the new iceberg module on the response of the AMOC to prescribed iceberg hosing versus hosing with freshwater in an ensemble of multi-millennial simulations under preindustrial forcing. The main results can be summarized as follows:

1. The spatial distribution of the meltwater flux in the North Atlantic has a marked effect on the strength of the AMOC response. The more meltwater that reaches the sites where NADW is formed, the stronger is the AMOC response.
2. Point source iceberg discharge in front of Hudson Strait has a larger effect on the AMOC than an equivalent localized freshwater hosing. Thus, the latter method leads to an underestimation of the AMOC response.
3. Latitude belt freshwater hosing on the other hand leads to an overestimation of the AMOC sensitivity, as the amount of direct meltwater forcing in the north east Atlantic is overestimated.
4. The cooling of the ocean, due to the latent heat of melting icebergs, strongly reduces the melt near the calving site. This contributes to a longer lifetime of icebergs. The destabilization of the AMOC, due to the larger meltwater input into the northeast Atlantic, is largely compensated by the stabilizing effect of colder SSTs. Thus the total effect of the latent heat coupling on the AMOC sensitivity is rather small.

The key results obtained from our simulations highlight the importance of including interactive icebergs in long-term climate simulations. This is particularly true during periods of considerably discharge from ice sheets (e.g., HEs or the deglaciation), as solid and liquid discharge have different effects on the climate. Hence, the new iceberg module has been incorporated into a coupled atmosphere-ocean-ice-sheet model set-up aimed at long-term climate simulations (like the deglaciation) within the last glacial cycle (www.pal-mod.de).

In the present version of our iceberg module the size distribution for present-day Greenland has been applied globally. For Antarctica it is known that calving of big tabular icebergs can occur. Including this and different size distributions for Greenland and Antarctica could easily be implemented. Also an extension into a two-dimensional size distribution (area and height) is straightforward and could be implemented in the future. For strong discharge events it might be useful to prevent icebergs from covering more than 100% of the grid area. The iceberg module could also be advanced by improving the physics, for example, by accounting for huge icebergs and their breakup (England et al., 2020; Huth, Adcroft, & Sergienko, 2022; Huth, Adcroft, Sergienko, & Khan, 2022; Stern et al., 2017).

Appendix A: Supplementary Materials

Here we include supporting materials for our experiments. Tables A1 and A2 show iceberg meltwater flux simulated for present day by Lagrangian iceberg module in Southern (Figure A1) and Northern (Figure A2) hemispheres by Martin and Adcroft (2010) and Merino et al. (2016). Figure A3 shows AMOC strength in the experimental set up as in Stouffer et al. (2006) with an input rate of 0.1 Sv distributed between 50° and 70°N. Figure A4 shows AMOC strength versus input rate for the experiment where the input rate was slowed down to 0.0333 Sv in 1,000 years. Figure A5 Shows Atlantic stream function before (left) and after (right) the AMOC collapse in the iceberg experiment.

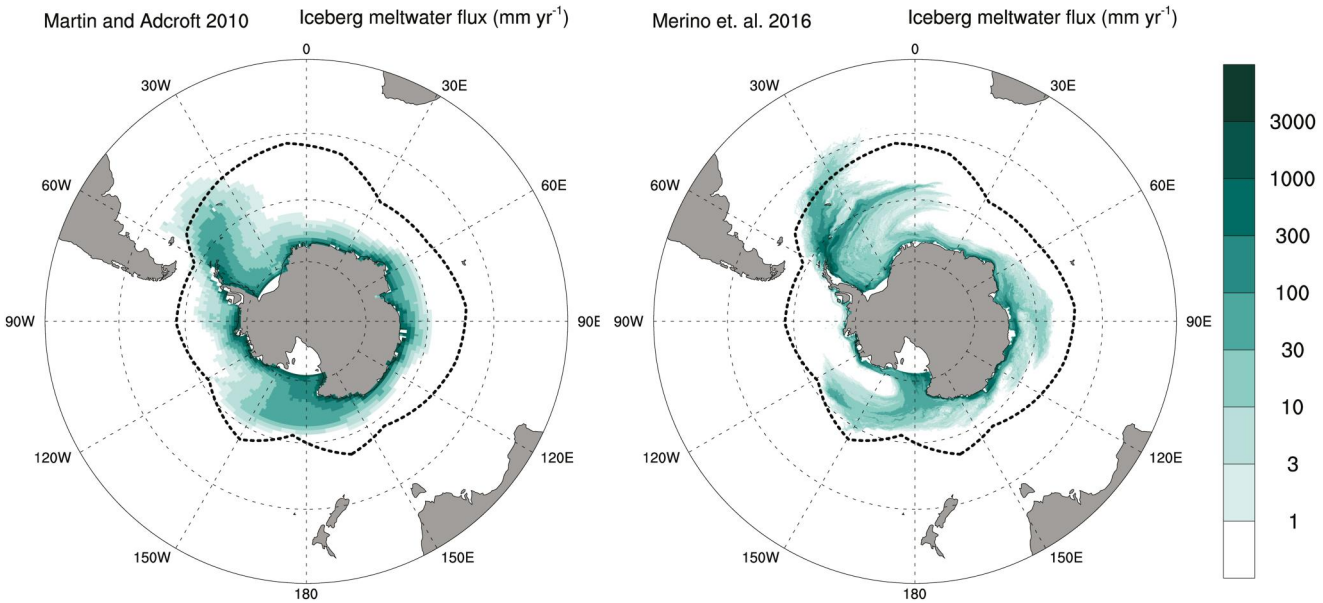

Figure A1. Simulated iceberg meltwater flux (mm yr^{-1}). Annual calving flux is 2,000 Gt yr^{-1} (left, Martin & Adcroft, 2010), 1,380 Gt yr^{-1} (right, Merino et al., 2016). Black dashed lines denote the observed iceberg extent (Jongma et al., 2009).

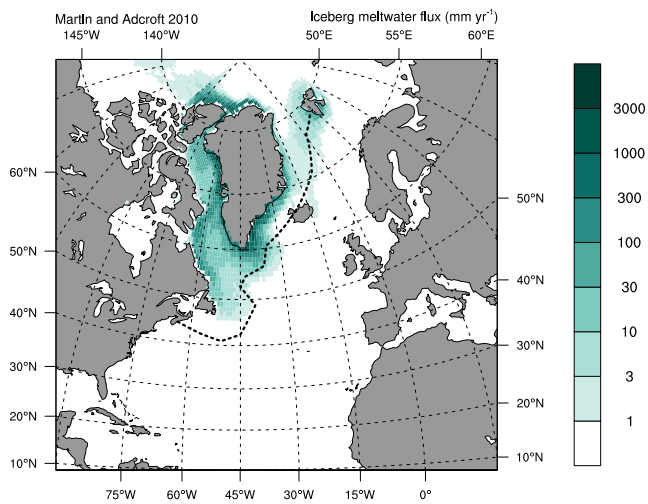

Figure A2. Simulated iceberg meltwater flux (mm yr^{-1}) in the Northern Hemisphere from Martin and Adcroft (2010). Annual calving flux is 210 Gt yr^{-1}.

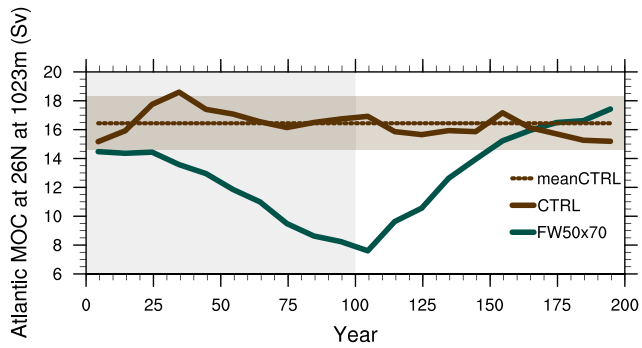

Figure A3. Atlantic meridional overturning circulation (AMOC) strength at 26°N at 1,023 m (Sv) in experiment CTRL (brown) and FW50x70x01Sv (experiment set up is similar to Stouffer et al. (2006) where the constant freshwater input rate of 0.1 Sv is added between 50° an 70°N). Brown dotted line corresponds to AMOC mean strength of the first 200 years of CTRL experiment, brown shaded area denotes twofold decadal standard deviation, gray shaded area denotes 100-year freshwater hosing period.

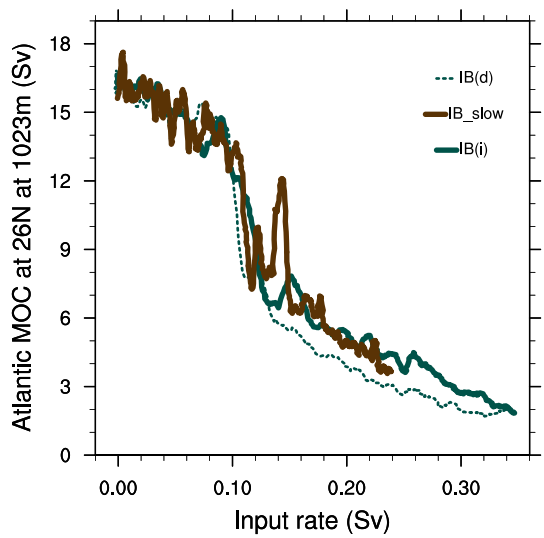

Figure A4. Atlantic meridional overturning circulation at 1,023 m at 26°N (Sv) versus input rate (Sv) in experiments IB (0.1 Sv in 1,000 years input rate increase) and IB_slow (0.0333 Sv in 1,000 years input rate increase). Solid lines (i) depict the first part of experiments when input rate increases; dashed lines (d) correspond to the second part of experiments when input rate decreases in IB.

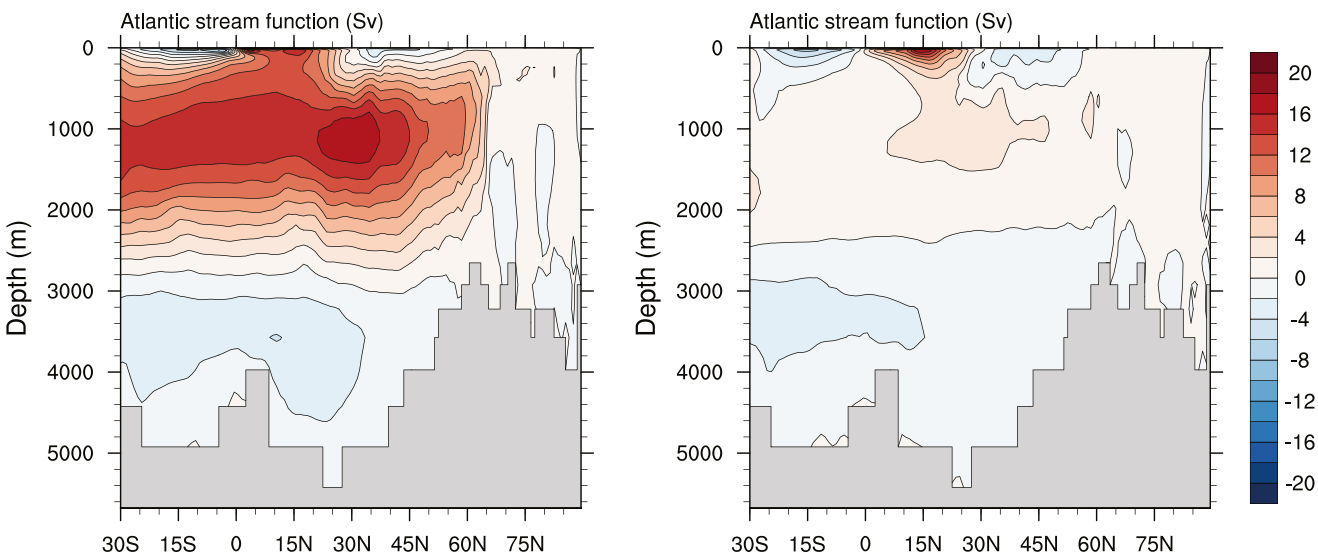

Figure A5. Atlantic meridional overturning circulation stream function (Sv) before and after the collapse in IB experiment.

Table A1
Computational Time of Eulerian Iceberg Module as a Fraction of the Total Model Computational Cost for Different Number of Iceberg Size Classes N *in GR15*

N	Computational time as a part of total (%)
02	3.70
03	5.00
05	8.21
09	14.86
17	23.81

Table A2
Abbreviations

Symbol	Description
1D	One dimensional
2D	Two dimensional
3D	Three dimensional
AMOC	Atlantic meridional overturning circulation
CMIP	Climate Model Intercomparison Project
CR	Coarse Resolution
ECHAM6	Atmospheric component of MPI-ESM
ESM	Earth System Model
JSBACH	Land component of MPI-ESM
HE	Heinrich Event
HD	the river runoff module in MPI-ESM
LGM	Last Glacial Maximum
MPI-ESM	Max Planck Institute Earth System Model
MPIOM	Ocean component of MPI-ESM
NADW	North Atlantic deep water
OASIS3	The atmosphere and the ocean coupler in MPI-ESM
SSS	Sea Surface Salinity
SST	Sea Surface Temperature

Acknowledgments
This work was supported by the Max Planck Society for the Advancement of Science and the International Max Planck Research School on Earth System Modelling. All model simulations and analyses were performed using resources of the German Climate Computing Center (DKRZ). This study benefited from cooperation with the PalMOD project. We benefited from discussions with Torge Martin, which were very helpful for the development of our iceberg module. We would like to thank Marie-Luise Kapsch, Clemens Schannwell, and three anonymous reviewers for useful comments that significantly improved the manuscript. We would like to thank Katharina Six for the support on coupling the iceberg module into the MPI-ESM. Open Access funding enabled and organized by Projekt DEAL.

Data Availability Statement

Model data and scripts used for the analysis, as well as Eulerian iceberg code are available online on the MPG. PuRe repository (https://pure.mpg.de/pubman/faces/ViewItemOverviewPage.jsp?itemId=item_3502496_6). MPI-ESM model code is available upon request from the Max Planck Institute for Meteorology under the Software License Agreement version 2 (https://code.mpimet.mpg.de/projects/mpi-esm-license). Raw model output is available online on the DKRZ long term archive (Erokhina & Mikolajewicz, 2023a, https://hdl.handle.net/21.14106/818d45326c9aaf7327704d433eedd6a172dd7163 and Erokhina & Mikolajewicz, 2023b, https://hdl.handle.net/21.14106/a75749d3791fb581c07ce308fa2a761a5cc1eb86).

References

Andrews, J. T., & Voelker, A. H. (2018). "Heinrich events" (& sediments): A history of terminology and recommendations for future usage. *Quaternary Science Reviews*, *187*, 31–40. https://doi.org/10.1016/j.quascirev.2018.03.017

Arakawa, A., & Lamb, V. R. (1977). Computational design of the basic dynamical processes of the UCLA general circulation model. *General circulation models of the atmosphere*, *17*, 173–265.

Berger, A., & Loutre, M.-F. (1991). Insolation values for the climate of the last 10 million years. *Quaternary Science Reviews*, *10*(4), 297–317. https://doi.org/10.1016/0277-3791(91)90033-q

Bigg, G. R., Cropper, T., O'Neill, C. K., Arnold, A. K., Fleming, A. H., Marsh, R., et al. (2018). A model for assessing iceberg hazard. *Natural Hazards*, *92*(2), 1–24. https://doi.org/10.1007/s11069-018-3243-x

Bigg, G. R., Levine, R. C., & Green, C. L. (2011). Modelling abrupt glacial North Atlantic freshening: Rates of change and their implications for heinrich events. *Global and Planetary Change*, *79*(3–4), 176–192. https://doi.org/10.1016/j.gloplacha.2010.11.001

Bigg, G. R., Wadley, M. R., Stevens, D. P., & Johnson, J. A. (1997). Modelling the dynamics and thermodynamics of icebergs. *Cold Regions Science and Technology*, *26*(2), 113–135. https://doi.org/10.1016/s0165-232x(97)00012-8

Bigg, G. R., & Wilton, D. J. (2014). Iceberg risk in the Titanic year of 1912: Was it exceptional? *Weather*, *69*(4), 100–104. https://doi.org/10.1002/wea.2238

Broecker, W. S. (1990). Salinity history of the northern Atlantic during the last deglaciation. *Paleoceanography*, *5*(4), 459–467. https://doi.org/10.1029/PA005i004p00459

Bryden, H. L., Johns, W. E., King, B. A., McCarthy, G., McDonagh, E. L., Moat, B. I., & Smeed, D. A. (2020). Reduction in ocean heat transport at 26 n since 2008 cools the eastern subpolar gyre of the North Atlantic Ocean. *Journal of Climate*, *33*(5), 1677–1689. https://doi.org/10.1175/jcli-d-19-0323.1

Bügelmayer, M., Roche, D., & Renssen, H. (2015). Representing icebergs in the i LOVECLIM model (version 1.0)—A sensitivity study. *Geoscientific Model Development*, *8*(7), 2139–2151. https://doi.org/10.5194/gmd-8-2139-2015

Comeau, D. (2013). *Conceptual and numerical modeling of ice in a global climate framework*. The University of Arizona.

Condron, A., & Winsor, P. (2012). Meltwater routing and the younger dryas. *Proceedings of the National Academy of Sciences*, *109*(49), 19928–19933. https://doi.org/10.1073/pnas.1207381109

Dowdeswell, J. A., & Forsberg, C. F. (1992). The size and frequency of icebergs and bergy bits derived from tidewater glaciers in kongsfjorden, northwest spitsbergen. *Polar Research*, *11*(2), 81–91. https://doi.org/10.3402/polar.v11i2.6719

El-Tahan, M., Venkatesh, S., & El-Tahan, H. (1987). Validation and quantitative assessment of the deterioration mechanisms of Arctic icebergs. *Journal of Offshore Mechanics and Arctic Engineering*, *109*(1), 102–108. https://doi.org/10.1115/1.3256983

England, M. R., Wagner, T. J., & Eisenman, I. (2020). Modeling the breakup of tabular icebergs. *Science Advances*, *6*(51), eabd1273. https://doi.org/10.1126/sciadv.abd1273

Erokhina, O., & Mikolajewicz, U. (2023a). MPI-ESM-Iberg experiments. DOKU at DKRZ. Retrieved from https://hdl.handle.net/21.14106/818d45326c9aaf7327704d433eedd6a172dd7163

Erokhina, O., & Mikolajewicz, U. (2023b). MPI-OM-Iberg experiments. DOKU at DKRZ. Retrieved from https://hdl.handle.net/21.14106/a75749d3791fb581c07ce308fa2a761a5cc1eb86

Fendrock, M., Condron, A., & McGee, D. (2022). Modeling iceberg longevity and distribution during heinrich events. *Paleoceanography and Paleoclimatology*, *37*(6), e2021PA004347. https://doi.org/10.1029/2021pa004347

Flato, G., Marotzke, J., Abiodun, B., Braconnot, P., Chou, S., Collins, W., et al. (2013). Climate change 2013: The physical science basis. In T. F. Stocker, D. Qin, G.-K. Plattner, M. Tignor, S. K. Allen, J. Boschung, et al. (Eds.), *Contribution of working group i to the fifth assessment report of the intergovernmental panel on climate change. Evaluation of Climate Models*. Cambridge University Press.

Frajka-Williams, E., Ansorge, I. J., Baehr, J., Bryden, H. L., Chidichimo, M. P., Cunningham, S. A., et al. (2019). Atlantic meridional overturning circulation: Observed transport and variability. *Frontiers in Marine Science*, *6*, 260. https://doi.org/10.3389/fmars.2019.00260

Ganopolski, A., & Rahmstorf, S. (2001). Rapid changes of glacial climate simulated in a coupled climate model. *Nature*, *409*(6817), 153–158. https://doi.org/10.1038/35051500

Gladstone, R. M., Bigg, G. R., & Nicholls, K. W. (2001). Iceberg trajectory modeling and meltwater injection in the Southern Ocean. *Journal of Geophysical Research*, *106*(C9), 19903–19915. https://doi.org/10.1029/2000jc000347

Gregory, J., Saenko, O., & Weaver, A. (2003). The role of the Atlantic freshwater balance in the hysteresis of the meridional overturning circulation. *Climate Dynamics*, *21*(7–8), 707–717. https://doi.org/10.1007/s00382-003-0359-8

Hagemann, S., & Dümenil, L. (1997). A parametrization of the lateral waterflow for the global scale. *Climate Dynamics*, *14*(1), 17–31. https://doi.org/10.1007/s003820050205

Heinrich, H. (1988). Origin and consequences of cyclic ice rafting in the northeast Atlantic Ocean during the past 130,000 years. *Quaternary Research*, *29*(2), 142–152. https://doi.org/10.1016/0033-5894(88)90057-9

Hibler, W. D. (1979). A dynamic thermodynamic Sea Ice model. *Journal of Physical Oceanography*, *9*(4), 815–846. https://doi.org/10.1175/1520-0485(1979)009<0815:ADTSIM>2.0.CO;2

Hu, A., Meehl, G. A., Abe-Ouchi, A., Han, W., Otto-Bliesner, B., He, F., et al. (2023). Dichotomy between freshwater and heat flux effects on oceanic conveyor belt stability and global climate. *Communications Earth & Environment*, *4*(1), 246. https://doi.org/10.1038/s43247-023-00916-0

Hunke, E. C., & Comeau, D. (2011). Sea ice and iceberg dynamic interaction. *Journal of Geophysical Research*, *116*(C5), C05008. https://doi.org/10.1029/2010jc006588

Hurrell, J. W., Hack, J. J., Shea, D., Caron, J. M., & Rosinski, J. (2008). A new sea surface temperature and sea ice boundary dataset for the community atmosphere model. *Journal of Climate*, *21*(19), 5145–5153. https://doi.org/10.1175/2008jcli2292.1

Huth, A., Adcroft, A., & Sergienko, O. (2022). Parameterizing tabular-iceberg decay in an ocean model. *Journal of Advances in Modeling Earth Systems*, *14*(3), e2021MS002869. https://doi.org/10.1029/2021ms002869

Huth, A., Adcroft, A., Sergienko, O., & Khan, N. (2022). Ocean currents break up a tabular iceberg. *Science Advances*, *8*(42), eabq6974. https://doi.org/10.1126/sciadv.abq6974

Ivanovic, R. F., Gregoire, L. J., Kageyama, M., Roche, D. M., Valdes, P. J., Burke, A., et al. (2016). Transient climate simulations of the deglaciation 21–9 thousand years before present (version 1)—PMIP4 core experiment design and boundary conditions. *Geoscientific Model Development*, *9*(7), 2563–2587. https://doi.org/10.5194/gmd-9-2563-2016

Jackson, L., & Wood, R. (2018). Hysteresis and resilience of the AMOC in an eddy-permitting gcm. *Geophysical Research Letters*, *45*(16), 8547–8556. https://doi.org/10.1029/2018gl078104

Jackson, L. C., Alastrué de Asenjo, E., Bellomo, K., Danabasoglu, G., Haak, H., Hu, A., et al. (2023). Understanding amoc stability: The North Atlantic hosing model intercomparison project. *Geoscientific Model Development*, *16*(7), 1975–1995. https://doi.org/10.5194/gmd-16-1975-2023

Jongma, J. I., Driesschaert, E., Fichefet, T., Goosse, H., & Renssen, H. (2009). The effect of dynamic–thermodynamic icebergs on the Southern Ocean climate in a three-dimensional model. *Ocean Modelling*, *26*(1–2), 104–113. https://doi.org/10.1016/j.ocemod.2008.09.007

Jongma, J. I., Renssen, H., & Roche, D. M. (2013). Simulating Heinrich event 1 with interactive icebergs. *Climate Dynamics*, *40*(5–6), 1373–1385. https://doi.org/10.1007/s00382-012-1421-1

Jungclaus, J., Fischer, N., Haak, H., Lohmann, K., Marotzke, J., Matei, D., et al. (2013). Characteristics of the ocean simulations in the Max Planck Institute Ocean Model (MPIOM) the ocean component of the MPI-Earth system model. *Journal of Advances in Modeling Earth Systems*, *5*(2), 422–446. https://doi.org/10.1002/jame.20023

Jungclaus, J., Keenlyside, N., Botzet, M., Haak, H., Luo, J.-J., Latif, M., et al. (2006). Ocean circulation and tropical variability in the coupled model ECHAM5/MPI-OM. *Journal of Climate*, *19*(16), 3952–3972. https://doi.org/10.1175/jcli3827.1

Kageyama, M., Merkel, U., Otto-Bliesner, B., Prange, M., Abe-Ouchi, A., Lohmann, G., et al. (2013). Climatic impacts of fresh water hosing under last glacial maximum conditions: A multi-model study. *Climate of the Past*, *9*(2), 935–953. https://doi.org/10.5194/cp-9-935-2013

Kapsch, M.-L., Mikolajewicz, U., Ziemen, F., & Schannwell, C. (2022). Ocean response in transient simulations of the last deglaciation dominated by underlying ice-sheet reconstruction and method of meltwater distribution. *Geophysical Research Letters*, *49*(3), e2021GL096767. https://doi.org/10.1029/2021gl096767

Kapsch, M.-L., Mikolajewicz, U., Ziemen, F. A., Rodehacke, C. B., & Schannwell, C. (2020). Analysis of the surface mass balance for deglacial climate simulations. In *The cryosphere discussions* (pp. 1–40).

Keghouche, I., Bertino, L., & Lisæter, K. A. (2009). Parameterization of an iceberg drift model in the Barents Sea. *Journal of Atmospheric and Oceanic Technology*, *26*(10), 2216–2227. https://doi.org/10.1175/2009jtecho678.1

Köhler, P., Nehrbass-Ahles, C., Schmitt, J., Stocker, T. F., & Fischer, H. (2017). A 156 kyr smoothed history of the atmospheric greenhouse gases CO_2, CH_4, and N_2O and their radiative forcing. *Earth System Science Data*, *9*(1), 363–387. https://doi.org/10.5194/essd-9-363-2017

Kubat, I., Sayed, M., Savage, S. B., Carrieres, T., & Crocker, G. (2007). An operational iceberg deterioration model. In *The seventeenth international offshore and polar engineering conference*.

Kuniyoshi, Y., Abe-Ouchi, A., Sherriff-Tadano, S., Chan, W.-L., & Saito, F. (2022). Effect of climatic precession on dansgaard-oeschger-like oscillations. *Geophysical Research Letters*, *49*(6), e2021GL095695. https://doi.org/10.1029/2021GL095695

Lazier, J. R. N. (1994). Observations in the northwest corner of the North Atlantic current. *Journal of Physical Oceanography*, *24*(7), 1449–1463. https://doi.org/10.1175/1520-0485(1994)024⟨1449:OITNCO⟩2.0.CO;2

Levine, R. C., & Bigg, G. R. (2008). Sensitivity of the glacial ocean to Heinrich events from different iceberg sources, as modeled by a coupled atmosphere-iceberg-ocean model. *Paleoceanography and Paleoclimatology*, *23*(4), PA4213. https://doi.org/10.1029/2008pa001613

Locarnini, M., Mishonov, A., Baranova, O., Boyer, T., Zweng, M., Garcia, H., et al. (2018). World ocean atlas 2018, volume 1: Temperature.

Love, R., Andres, H. J., Condron, A., & Tarasov, L. (2021). Freshwater routing in eddy-permitting simulations of the last deglacial: The impact of realistic freshwater discharge. *Climate of the Past*, *17*(6), 2327–2341. https://doi.org/10.5194/cp-17-2327-2021

Maier-Reimer, E., & Mikolajewicz, U. (1989). *Experiments with an OGCM on the cause of the Younger Dryas*. Max-Planck-Institut für Meteorologie Hamburg.

Malmierca-Vallet, I., Sime, L. C., & the D-O Community Members. (2022). Dansgaard-Oeschger events in climate models: Review and baseline MIS3 protocol. *EGUsphere*, 1–45. https://doi.org/10.5194/egusphere-2022-707

Marsh, R., Ivchenko, V., Skliris, N., Alderson, S., Bigg, G. R., Madec, G., et al. (2015). NEMO–ICB (v1. 0): Interactive icebergs in the NEMO ocean model globally configured at eddy-permitting resolution. *Geoscientific Model Development*, *8*(5), 1547–1562. https://doi.org/10.5194/gmd-8-1547-2015

Marsland, S. J., Haak, H., Jungclaus, J. H., Latif, M., & Röske, F. (2003). The Max-Planck-Institute global ocean/sea ice model with orthogonal curvilinear coordinates. *Ocean Modelling*, *5*(2), 91–127. https://doi.org/10.1016/s1463-5003(02)00015-x

Marson, J. M., Gillard, L. C., & Myers, P. G. (2021). Distinct ocean responses to Greenland's liquid runoff and iceberg melt. *Journal of Geophysical Research: Oceans*, *126*(12), e2021JC017542. https://doi.org/10.1029/2021jc017542

Martin, T., & Adcroft, A. (2010). Parameterizing the fresh-water flux from land ice to ocean with interactive icebergs in a coupled climate model. *Ocean Modelling*, *34*(3–4), 111–124. https://doi.org/10.1016/j.ocemod.2010.05.001

Martin, T., Biastoch, A., Lohmann, G., Mikolajewicz, U., & Wang, X. (2022). On timescales and reversibility of the ocean's response to enhanced Greenland ice sheet melting in comprehensive climate models. *Geophysical Research Letters*, *49*(5), e2021GL097114. https://doi.org/10.1029/2021GL097114

Mauritsen, T., Bader, J., Becker, T., Behrens, J., Bittner, M., Brokopf, R., et al. (2019). Developments in the MPI-M earth system model version 1.2 (MPI-ESM1.2) and its response to increasing CO_2. *Journal of Advances in Modeling Earth Systems*, *11*(4), 998–1038. https://doi.org/10.1029/2018ms001400

McCarthy, G. D., Smeed, D. A., Johns, W. E., Frajka-Williams, E., Moat, B. I., Rayner, D., et al. (2015). Measuring the Atlantic meridional overturning circulation at 26 n. *Progress in Oceanography*, *130*, 91–111. https://doi.org/10.1016/j.pocean.2014.10.006

Meccia, V. L., & Mikolajewicz, U. (2018). Interactive ocean bathymetry and coastlines for simulating the last deglaciation with the Max Planck institute earth system model (MPI-ESM-v1.2). *Geoscientific Model Development*, *11*, 4677–4692. https://doi.org/10.5194/gmd-11-4677-2018

Merino, N., Le Sommer, J., Durand, G., Jourdain, N. C., Madec, G., Mathiot, P., & Tournadre, J. (2016). Antarctic icebergs melt over the Southern Ocean: Climatology and impact on sea ice. *Ocean Modelling*, *104*, 99–110. https://doi.org/10.1016/j.ocemod.2016.05.001

Mikolajewicz, U., & Maier-Reimer, E. (1994). Mixed boundary conditions in ocean general circulation models and their influence on the stability of the model's conveyor belt. *Journal of Geophysical Research*, *99*(C11), 22633–22644. https://doi.org/10.1029/94jc01989

Mountain, D. (1980). On predicting iceberg drift. *Cold Regions Science and Technology*, *1*(3–4), 273–282. https://doi.org/10.1016/0165-232x(80)90055-5

Otto-Bliesner, B. L., & Brady, E. C. (2010). The sensitivity of the climate response to the magnitude and location of freshwater forcing: Last glacial maximum experiments. *Quaternary Science Reviews*, *29*(1–2), 56–73. https://doi.org/10.1016/j.quascirev.2009.07.004

Peltier, W. R., Vettoretti, G., & Stastna, M. (2006). Atlantic meridional overturning and climate response to Arctic Ocean freshening. *Geophysical Research Letters*, *33*(6), L06713. https://doi.org/10.1029/2005GL025251

Rackow, T., Wesche, C., Timmermann, R., Hellmer, H. H., Juricke, S., & Jung, T. (2017). A simulation of small to giant Antarctic iceberg evolution: Differential impact on climatology estimates. *Journal of Geophysical Research: Oceans*, *122*(4), 3170–3190. https://doi.org/10.1002/2016jc012513

Rahmstorf, S. (1996). On the freshwater forcing and transport of the Atlantic thermohaline circulation. *Climate Dynamics*, *12*(12), 799–811. https://doi.org/10.1007/s003820050144

Rahmstorf, S. (2002). Ocean circulation and climate during the past 120,000 years. *Nature*, *419*(6903), 207–214. https://doi.org/10.1038/nature01090

Reick, C., Raddatz, T., Brovkin, V., & Gayler, V. (2013). Representation of natural and anthropogenic land cover change in MPI-ESM. *Journal of Advances in Modeling Earth Systems*, *5*(3), 459–482. https://doi.org/10.1002/jame.20022

Riddick, T., Brovkin, V., Hagemann, S., & Mikolajewicz, U. (2018). Dynamic hydrological discharge modelling for coupled climate model simulations of the last glacial cycle: The MPI-DynamicHD model version 3.0. *Geoscientific Model Development*, *11*(10), 4291–4316. https://doi.org/10.5194/gmd-11-4291-2018

Rignot, E., Jacobs, S., Mouginot, J., & Scheuchl, B. (2013). Ice-shelf melting around Antarctica. *Science*, *341*(6143), 266–270. https://doi.org/10.1126/science.1235798

Roche, D. M., Paillard, D., Caley, T., & Waelbroeck, C. (2014). Lgm hosing approach to heinrich event 1: Results and perspectives from data–model integration using water isotopes. *Quaternary Science Reviews*, *106*, 247–261. https://doi.org/10.1016/j.quascirev.2014.07.020

Röske, F. (2001). *An Atlas of surface fluxes based on the ECMWF Re-analysis: A climatological dataset to force global ocean general circulation models*. Max-Planck-Institut für Meteorologie Hamburg.

Ruddiman, W. F. (1977). Late Quaternary deposition of ice-rafted sand in the subpolar North Atlantic (lat 40 to 65N). *Geological Society of America Bulletin*, *88*(12), 1813–1827. https://doi.org/10.1130/0016-7606(1977)88<1813:lqdois>2.0.co;2

Savage, S. (2001). Aspects of iceberg deterioration and drift. In *Geomorphological fluid mechanics* (pp. 279–318). Springer.

Schiller, A., Mikolajewicz, U., & Voss, R. (1997). The stability of the North Atlantic thermohaline circulation in a coupled ocean-atmosphere general circulation model. *Climate Dynamics*, *13*(5), 325–347. https://doi.org/10.1007/s003820050169

Schloesser, F., Friedrich, T., Timmermann, A., DeConto, R. M., & Pollard, D. (2019). Antarctic iceberg impacts on future southern hemisphere climate. *Nature Climate Change*, *9*(9), 672–677. https://doi.org/10.1038/s41558-019-0546-1

Schneck, R., Reick, C. H., & Raddatz, T. (2013). Land contribution to natural CO_2 variability on time scales of centuries. *Journal of Advances in Modeling Earth Systems*, *5*(2), 354–365. https://doi.org/10.1002/jame.20029

Shea, D., Hurrell, J., & Phillips, A. (2020). Merged hadley-OI sea surface temperature and sea ice concentration data set, version.

Smith, R. S., & Gregory, J. M. (2009). A study of the sensitivity of ocean overturning circulation and climate to freshwater input in different regions of the North Atlantic. *Geophysical Research Letters*, *36*(15), L15701. https://doi.org/10.1029/2009gl038607

Smith, S. D. (1993). Hindcasting iceberg drift using current profiles and winds. *Cold Regions Science and Technology*, *22*(1), 33–45. https://doi.org/10.1016/0165-232x(93)90044-9

Snoll, B., Ivanovic, R., Gregoire, L., Sherriff-Tadano, S., Menviel, L., Obase, T., et al. (2023). A multi-model assessment of the early last deglaciation (PMIP4 LDV1): The meltwater paradox reigns supreme. *EGUsphere*, *2023*, 1–45. https://doi.org/10.5194/egusphere-2023-1802

Stern, A., Adcroft, A., Sergienko, O., & Marques, G. (2017). Modeling tabular icebergs submerged in the ocean. *Journal of Advances in Modeling Earth Systems*, *9*(4), 1948–1972. https://doi.org/10.1002/2017ms001002

Stevens, B., Giorgetta, M., Esch, M., Mauritsen, T., Crueger, T., Rast, S., et al. (2013). Atmospheric component of the MPI-M earth system model: ECHAM6. *Journal of Advances in Modeling Earth Systems*, *5*(2), 146–172. https://doi.org/10.1002/jame.20015

Stommel, H. (1961). Thermohaline convection with two stable regimes of flow. *Tellus*, *13*(2), 224–230. https://doi.org/10.3402/tellusb.v13i2.12985

Stouffer, R. J., Yin, J., Gregory, J. M., Dixon, K. W., Spelman, M. J., Hurlin, W., et al. (2006). Investigating the causes of the response of the thermohaline circulation to past and future climate changes. *Journal of Climate*, *19*(8), 1365–1387. https://doi.org/10.1175/JCLI3689.1

Swingedouw, D., Houssais, M.-N., Herbaut, C., Blaizot, A.-C., Devilliers, M., & Deshayes, J. (2022). Amoc recent and future trends: A crucial role for oceanic resolution and Greenland melting? *Frontiers in Climate*, *4*, 32. https://doi.org/10.3389/fclim.2022.838310

Swingedouw, D., Rodehacke, C. B., Olsen, S. M., Menary, M., Gao, Y., Mikolajewicz, U., & Mignot, J. (2015). On the reduced sensitivity of the Atlantic overturning to Greenland ice sheet melting in projections: A multi-model assessment. *Climate Dynamics*, *44*(11–12), 3261–3279. https://doi.org/10.1007/s00382-014-2270-x

Tarasov, L., Dyke, A. S., Neal, R. M., & Peltier, W. R. (2012). A data-calibrated distribution of deglacial chronologies for the North American ice complex from glaciological modeling. *Earth and Planetary Science Letters*, *315*, 30–40. https://doi.org/10.1016/j.epsl.2011.09.010

Tournadre, J. (2022). Database of small icebergs from satellite altimetry for altiberg project. ver. 3.1. Ifremer, Plouzane, France. https://doi.org/10.12770/06770b5a-b8aa-4a59-b66d-304c2bf9b548

Tournadre, J., Bouhier, N., Girard-Ardhuin, F., & Rémy, F. (2016). Antarctic icebergs distributions 1992–2014. *Journal of Geophysical Research: Oceans*, *121*(1), 327–349. https://doi.org/10.1002/2015JC011178

Turnbull, I. D., Fournier, N., Stolwijk, M., Fosnaes, T., & McGonigal, D. (2015). Operational iceberg drift forecasting in Northwest Greenland. *Cold Regions Science and Technology*, *110*, 1–18. https://doi.org/10.1016/j.coldregions.2014.10.006

Valcke, S. (2013). The OASIS3 coupler: A European climate modelling community software. *Geoscientific Model Development*, *6*(2), 373–388. https://doi.org/10.5194/gmd-6-373-2013

Vaňková, I., & Holland, D. M. (2017). A model of icebergs and sea ice in a joint continuum framework. *Journal of Geophysical Research: Oceans*, *122*(11), 9110–9125. https://doi.org/10.1002/2017jc013012

Wagner, T. J., Dell, R. W., & Eisenman, I. (2017). An analytical model of iceberg drift. *Journal of Physical Oceanography*, *47*(7), 1605–1616. https://doi.org/10.1175/jpo-d-16-0262.1

Weeks, W., & Mellor, M. (1978). Some elements of iceberg technology, crrel report.

Wiersma, A. P., & Jongma, J. I. (2010). A role for icebergs in the 8.2 ka climate event. *Climate Dynamics*, *35*(2–3), 535–549. https://doi.org/10.1007/s00382-009-0645-1

Ziemen, F., Kapsch, M.-L., Klockmann, M., & Mikolajewicz, U. (2019). Heinrich events show two-stage climate response in transient glacial simulations. *Climate of the Past*, *15*(1), 153–168. https://doi.org/10.5194/cp-15-153-2019

Ziemen, F., Rodehacke, C., & Mikolajewicz, U. (2014). Coupled ice sheet–climate modeling under glacial and pre-industrial boundary conditions. *Climate of the Past*, *10*(5), 1817–1836. https://doi.org/10.5194/cp-10-1817-2014

Zweng, M., Seidov, D., Boyer, T., Locarnini, M., Garcia, H., Mishonov, A., et al. (2019). World ocean atlas 2018, volume 2: Salinity.